



Single-atom catalysis for carbon dioxide dissociation using greigite-supported $M_1/\text{Fe}_3\text{S}_4(111)$ ($M = \text{Sc}, \text{Ti}, \text{V}, \text{Cr}, \text{Mn}, \text{Fe}, \text{Co}, \text{Ni}, \text{Cu}, \text{Zn}$) under electrostatic fields



David Santos-Carballal^{a,*}, Nora H. de Leeuw^{a,b}

^aSchool of Chemistry, University of Leeds, Leeds LS2 9JT, United Kingdom

^bDepartment of Earth Sciences, Utrecht University, Princetonplein 8A, 3584 CD Utrecht, The Netherlands

ARTICLE INFO

Article history:

Received 30 January 2023

Revised 1 May 2023

Accepted 17 May 2023

Available online 22 May 2023

Keywords:

Thiospinels

Iron Sulfides

Density Functional Theory (DFT)

Minimum Energy Pathways (MEP)

Single-Atom Catalyst (SAC)

Transverse Electrostatic Fields

Carbon Dioxide (CO_2) Dissociation

ABSTRACT

Single transition metal adatoms (M) supported on a solid surface – here the reactive greigite $\text{Fe}_3\text{S}_4(111)$ surface – combine the best properties of homogeneous and heterogeneous catalytic systems and are highly selective materials capable of altering the pathway of difficult reactions. We have employed state-of-the-art first-principles simulations to investigate the process of carbon dioxide (CO_2) dissociation on the single-atom catalyst (SAC) $M_1/\text{Fe}_3\text{S}_4(111)$. We discuss how reconstructions of the symmetrical stacking sequence of charged atomic planes determines the possible stable non-polar terminations of the $\text{Fe}_3\text{S}_4(111)$ surface. The thermodynamic stability and the work function are the main descriptors that are affected by external electrostatic fields, both for the most stable termination of the pristine $\text{Fe}_3\text{S}_4(111)$ surface as well as the $M_1/\text{Fe}_3\text{S}_4(111)$ catalysts. We present the electron density plots for the $M_1/\text{Fe}_3\text{S}_4(111)$ surfaces, which show that the M adatom forms covalent metal-support interactions (CMSI). In general, positive external electrostatic fields enhance the adsorption properties of the $M_1/\text{Fe}_3\text{S}_4(111)$ catalysts towards the CO_2 molecule, which activates chemically upon interaction. Our energy profiles for the dissociation of the CO_2 molecule show that carefully selected transition metal adatoms, such as V, Cr and Co, and positive external electrostatic fields can be used to tune the catalytic properties of SACs.

© 2023 The Authors. Published by Elsevier Inc. This is an open access article under the CC BY license (<http://creativecommons.org/licenses/by/4.0/>).

1. Introduction

Single-atom catalysts (SAC), which consist of identical and uniformly dispersed monoatomic transition metal (M_1) active sites deposited on a support [1–3], display exceptionally good efficiency [4], selectivity and activity towards targeted chemical reactions [5–9]. The most extensively investigated substrates used to stabilise the active sites are high surface area metal oxides, such as the reducible oxides Fe_3O_4 [10–17], Fe_2O_3 [18,19], FeO_x [3,20–24], CeO_2 [25–30], MnO_2 [31–36], CoO_x [37–43], NiO [44], CuO [45,46], Cu_2O [47], ZnO [48–52], and photoactive TiO_2 [53–57], and irreducible oxides MgO [58–62], Al_2O_3 [63–67] and SiO_2 [68–72], as well as zeolites [73–77], metal-organic frameworks (MOFs) [78] and single-layered materials [79–81]. The single atom represents the limit of the smallest possible dimension of a nanoparticle, with the largest theoretical surface area to volume ratio, bringing the

discipline of heterogeneous catalysis closer to homogeneous and enzymatic catalysis, where the only active site is exposed [82–86]. The archetypal SACs are based on single, often noble, metal atoms Pd [15,17], Pt [3,14,16,18,24], Au [10,12,13,21,87], Ir [20,44,62,88,89], Rh [90–93] and Ag [31–33,35,36], other transition metal atoms such as Ni [94–96], Cu [94,97–100], V [56,94,101], Cr [55,94], Fe [53,54,94,102,103], Mn [94], Co [94,104–107], Mo [19,69,76,94,108], Os [109], Ti [70,77], Ta [110] and Re [71], W in the form of WO_x species [111], and even alkali metals [31,34]. Single-atom promoters La [63,112], Sn [113,114] and Zn [115], Ni [116], Cu [117], Zr [118] are considered a special type of SAC and are used to enhance the catalytic activity of metal nanoparticles or to stabilise their interface with the metal oxide substrate [8]. Exotic inverse SACs have been prepared by selectively depositing metal (hydr)oxide species containing a single metal atom, e.g. $\text{Fe}_1(\text{OH})_x$ [119] and MoO_x [108], on top of Pt nanoparticles stabilised over an oxide support, such as SiO_2 or WO_x . Single-atom alloy (SAA) catalysts, which are formed by depositing isolated metal atoms of catalytically active elements on the surface of a less active

* Corresponding author.

E-mail addresses: D.Santos-Carballal@leeds.ac.uk (D. Santos-Carballal), N.H.deLeeuw@leeds.ac.uk, N.H.deLeeuw@uu.nl (N.H. de Leeuw).

but more selective metal host, have also emerged as an important class of SACs [120–122].

The catalytic activity and selectivity of SACs is strongly linked to the nature of specific single atoms and to the particular chemical environment of the coordination sites in the support [83]. Tailored SACs have been developed for applications in well-established fields such as thermo-, electro- and photo-catalysts, as well as for the more contemporary multistep cascade reactions. Examples of thermo-catalytic applications include the water–gas shift reaction [123–125], preferential CO oxidation [3,29,119], selective oxidation of alkane to alcohols [102,126,127] and from the latter to aldehydes [21,128], selective hydrogenation of unsaturated C–C bonds [120,129,130], as well as coupling reactions between two C atoms [131–133] and between one C atom and one heteroatom [134–136]. The most important single-atom electro-catalysts (SAECs) uses are for the hydrogen evolution reaction (HER) [137–139], oxygen evolution reaction (OER) [140–142], oxygen reduction reaction (ORR) [143–145], carbon dioxide reduction reaction (CO₂RR) [146–148] and nitrogen reduction reaction (NRR) [149–151]. SACs have also been applied with significant success in several photo-catalytic processes comprising, for example, water splitting [152–154], carbon dioxide (CO₂) reduction [107,155,156], dinitrogen fixation [157,158], organic synthesis [159] and environmental remediation [160–162]. Rh and Ru SACs have been used for the one-pot cooperative tandem olefin isomerization-hydrosilylation process, whereas single Co sites dispersed on a Ti MOF catalyse the cascade reduction of N-heteroarenes [163].

The cubane-structured active sites of greigite (Fe₃S₄), which is the sulfide counterpart of the industrial catalyst magnetite (Fe₃O₄), have been associated with several hypotheses for the origin of life [164,165]. This theory was subsequently tested in a pilot study which showed that slightly acidic conditions were required for the adsorption and reduction of CO₂ into small soluble organic molecules over the catalytically active Fe₃S₄(111) surface [166]. Further investigations have indicated that the Fe₃S₄(111) facet is also capable of catalysing the direct combination of C1 species of different composition to produce acetic acid (CH₃COOH) via a glyoxylic acid intermediate (CHOCOOH) [167]. The Fe₃S₄(111) surface was found to preferentially reduce the carbon monoxide (CO) molecule to methanol (CH₃OH) [168], but it was unable to catalyse the dissociation of adsorbed water (H₂O) [169] or become reduced by hydrogen [170]. Studies into the nature of the Fe₃S₄ surfaces in the presence of water [171] and during the electrochemical H₂ evolution and CO₂ reduction reactions have found that this material forms core–shell iron sulfide/iron hydroxide nanoparticles [172]. This partial oxidation of the surfaces of sulfide materials has been shown to increase the catalytic activity with respect to the pristine surface towards the conversion of CO₂ into formate (HCOO[−]) [173] and oxalic acid (H₂C₂O₄) [174].

The use of transverse electrostatic fields has been shown to reduce the band gap of catalytic systems, including carbon nanotubes and boron nitride nanotubes. The electrostatic field is able to combine the band levels in the valence and conduction bands individually, making the band gap value dependent on the electrostatic field [175]. Internal electrostatic fields caused by the co-adsorption of ions on metal surfaces can dictate significant changes in the rate of heterogeneous catalytic processes [176], whereas external electrostatic fields can be used in so-called field-assisted catalysis, which is particularly suited to experimental investigation by pulsed field mass desorption spectroscopy, complemented computationally by density functional theory (DFT) calculations [177].

Anthropogenic CO₂, which is a pollutant produced in large quantities by the combustion of fossil fuels, can be harnessed as an alternative C1 carbon feedstock [178]. Carbon dioxide is currently utilised directly in strongly exergonic to moderately ender-

gonic processes, where the entire CO₂ moiety is incorporated into the final product. In these thermal syntheses of commodity chemicals, such as urea (RHN)₂CO, salicylic acid (HOC₆H₄CO₂H) and inorganic carbonates, the C atom maintains its oxidation number of 4+ or is just reduced to 3+. There is also a growing global interest in very endergonic applications for CO₂ to produce chemicals, e.g., carboxylic acids (RCOOH), and in particular formic acid (HCOOH), polycarbonates (−ROCOO−), polyurethanes (−RNHCOOR'OCOR'−) and carbamates (RR'NCOOR'') and acrylates (RCH₂CHCOOR'R''), as well as fuels including CO, methanol (CH₃OH), methane (CH₄) and larger hydrocarbons. However, these processes, which can contribute to the recycling of CO₂, whilst also reducing our dependence on natural fossil fuel resources, require stable, efficient, active and selective heterogeneous catalysts to facilitate the reduction of the oxidation number of the C atom to 2+ or lower to form the desired product.

This work reports the novel use of SACs supported on a reactive surface of the iron sulfide material greigite, M₁/Fe₃S₄(111), where M is a 3d transition metal from groups III to XII of the periodic table, in a systematic investigation of the catalytic dissociation of CO₂ under the effect of external electrostatic fields. We have used unrestricted *ab initio* methods to study the thermodynamic stabilities and geometries, as well as the electronic and magnetic properties, of the non-polar terminations of the Fe₃S₄(111) surface. Next, we have simulated the deposition of the single transition metal atoms onto the surface and discussed the impact on the major properties of the pristine Fe₃S₄(111) surface. We have inspected the adsorption of CO₂ and evaluated the chemical activation at the catalytic M₁ sites in the absence and in the presence of transversal electrostatic fields. Finally, we have calculated the geometries and energy profiles for the dissociation reaction of the CO₂ molecule over the M₁/Fe₃S₄(111) catalyst.

2. Computational methods

2.1. Calculation details

The Vienna *Ab Initio* Simulation Package (VASP) [179–182] was used to simulate the pristine Fe₃S₄(111) surface and the M₁/Fe₃S₄(111) SACs, as well as the mechanistic pathways for the dissociation of the CO₂ molecule. We employed the strongly constrained and appropriately normed (SCAN) exchange–correlation functional [183], within the *meta*-generalized gradient approximation (*meta*-GGA), for all our spin-polarised DFT calculations. The projected augmented wave (PAW) method [184,185], including the non-spherical contributions of the density gradient within the one-centre terms, were used to model the frozen core electrons, their kinetic energy densities and their interaction with the valence states. The 3s3p3d4s levels of Sc, Ti and V; the 3p3d4s levels of Cr, Mn, Fe, Co, Ni and Cu; the 3d4s levels of Zn; the 2s2p levels of O and C; and 1s level of H were treated as valence states. We used the charge-dielectric function proposed by Kerker for the initial approximation of the charge densities [186], which included up to the *g* orbitals of the one-centre PAW charge densities and were subsequently mixed employing the Pulay method [187]. We used a combination of the blocked Davidson iteration scheme [188–190] for the initial phase of the diagonalisation of the Kohn-Sham (KS) Hamiltonian, followed by the residual minimization method direct inversion in the iterative subspace (RMM-DIIS) [187] until the energy difference in two consecutive self-consistent loop steps dropped below 10^{−5} eV. A kinetic energy cut-off of 400 eV was applied for the periodic plane-wave basis set used to expand the KS valence states. The D2 semiempirical method of Grimme was included in our calculations to correct the long-range dispersion interactions [191] and improve the de-

scription of non-bonded distances and non-covalent interaction energies [192–200]. The SCAN + U approach is known to be required for the appropriate simulation of the d electrons in transition metal atoms forming oxides [201,202] and sulfides [174] and to enhance the description of the structural, energetic and electronic properties of these materials. Thus, a simplified rotationally invariant GGA Hubbard parameter [203,204] $U_{\text{eff}} = 5.26$ eV for Fe was employed to enhance the simulation of the electron correlations in the $3d$ levels of the cations in the support of the catalyst [174]. This specific U_{eff} parameter was developed fully theoretically using the versatile and universal approach of Cococcioni and Gironcoli [205], which has been widely applied, e.g. in the simulation of both magnetic CrI₃ nano-ribbons [206] and TaS₂ [207] with the PBE GGA functional, as well as metal oxides with the SCAN *meta*-GGA functional [208]. However, no Hubbard Hamiltonian was employed for the d states of the transition metal adatoms, as they are already delocalised due to their low concentration [209]. The DFT + U method is not free from limitations, as U_{eff} values are developed by fitting to observables such as band gaps, magnetic moments and heats of oxidation or using the linear response approach. U_{eff} can take values between 0, i.e. no correction typically used for pure metals, to several eV for the transition metal atom in semiconducting or insulating oxides or in our context sulfides [210]. We are confident of the U_{eff} value that we developed for the lattice Fe ions, since it predicts well the main structural, electronic and magnetic properties of the bulk of Fe₃S₄ and the catalytic activity of the (111) surface for the conversion of CO₂ into oxalic acid [174]. However, with the lack of experimental information of the SACs investigated in this work, we do not feel it appropriate to employ an arbitrary U_{eff} value to describe the single transition metal adatom. If we consider that an isolated transition metal atom is supported over the Fe₃S₄(111) surface of our SAC systems, then we do not need to use U_{eff} value for the adatoms, which are catalytically active sites supported on stable and easy to separate heterogeneous catalysts. We consider that although not perfect, our approach captures the trends of the catalytic activity of the SAC under investigation here, which is usually the main objective in theoretical surface science and catalysis [211].

We used a Newton line optimiser, which is an efficient conjugate gradients method [212,213], to perform the geometry optimisations, which curvature was estimated using a finite difference step size of 5×10^{-3} Å and a maximum allowed step size $\lambda = 0.2$ Å. The geometry optimisations were considered converged when the Hellmann-Feynman forces on all atoms became smaller than $0.01 \text{ eV} \cdot \text{Å}^{-1}$. We confirmed that, within the methodology used in this study, the total electronic energy was converged to within 1 meV atom^{-1} .

2.2. Surface and molecular models

We used METADISE [214] to cut the Fe₃S₄ bulk and construct the (111) surface, which was modelled using the periodic p (2×1) supercell. A vacuum void of 18 Å was included in the direction perpendicular to the simulation cell to avoid interaction with the periodically repeated images while ensuring that the surface can hold the CO₂ molecule in any conformation. The stacking sequence of the (111) surface slabs consisted of four formula unit (f.u.) layers, which is equivalent to 13 atomic layers, with an area of 87.647 Å^2 . The ions in the two bottommost f.u. layers were fixed at their optimised bulk positions, whereas the ions in the two top f.u. exposed layers were allowed to move during geometry optimisations, to represent the bulk phase and surfaces, respectively. We used the Gaussian smearing [215–218], with a sigma value $\sigma = 0.01$ eV to determine the electronic partial occupancies during all our geometry optimisations. The electronic integrations of the pristine Fe₃S₄(111) surface and $M_1/\text{Fe}_3\text{S}_4(111)$ SAC were calculated

in the reciprocal space using Γ -centered Monkhorst–Pack (MP) grids [219] of $4 \times 2 \times 1$ k -points, in line with earlier works [167,220]. The simulation of the isolated CO₂ molecule was carried out considering only the Γ point of the Brillouin zone (BZ), using a cell with broken symmetry and a volume of 9240 Å^3 . We applied dipole corrections [221,222] parallel to the [111] direction of our surface slabs to correct the errors to the total energy introduced by the molecules interacting on the relaxed side of the SAC [167,171,173,174,192,195,220,223–232]. We tested the convergence of energy differences within 1 meV per atom using different numbers of relaxed and total atomic layers as well as vacuum thicknesses for our simulation supercell.

The external electrostatic fields were applied using the Neugebauer and Scheffler method [221]. The work function (ϕ) was obtained by subtracting the Fermi level of the slab (E_F) to the potential at the vacuum level (E_{vac}). The magnetic moments and effective Bader atomic charges were integrated within the atomic basins obtained using an enhanced grid of charge density values without lattice bias [233–235]. The climbing image nudged elastic band (cNEB) algorithm was used to simulate the saddle points and minimum energy pathways (MEP) connecting reactants and products [236,237]. The cNEB method has been widely employed in the simulation of the saddle point energies and structures as well as the MEPs of a number of heterogeneous catalytic reactions [167,171,173,192,220]. The MEP were calculated using five images, which were optimised globally employing the limited-memory Broyden–Fletcher–Goldfarb–Shannon (LBFGS) method [213,238]. Consecutive images were separated by no more than 0.6 Å across all our cNEB calculations, which was enough to resolve the curvature along the dissociation path of the CO₂ molecule. A single imaginary vibrational frequency along the reaction coordinate was used to confirm saddle points. The wavenumbers of the fundamental harmonic vibrational modes were calculated via the central finite differences method, where each atom was permitted to make small movements in the three Cartesian directions.

2.3. Surface energy diagrams

The adsorption energy (E_{ads}) was estimated using the equation,

$$E_{\text{ads}} = E_{\text{CO}_2+\text{SAC}} - E_{\text{CO}_2} - E_{\text{SAC}} \quad (1)$$

Where $E_{\text{CO}_2+\text{SAC}}$, E_{CO_2} and E_{SAC} refer to the energy of the SAC containing the CO₂ molecule, the energy of the isolated adsorbate molecule, and the energy of the pristine SAC surface, respectively, in their ground state configurations.

We used the energy of the saddle point (E_{SP}) and the energy of the adsorbed CO₂ molecule (E_{CO_2}) to obtain the activation energy as $E_a = E_{\text{SP}} - E_{\text{CO}_2}$. The energy of the elemental step (ΔE) was obtained as the difference of the energy of the products and the energy of the reactants. The energy diagrams were prepared using the most stable binding modes of the reactants, intermediates and final products, which were connected by saddle points and MEPs.

The charge density differences ($\Delta\rho$) were plotted as,

$$\Delta\rho = \rho_{\text{CO}_2+\text{SAC}} - \rho_{\text{CO}_2} - \rho_{\text{SAC}} \quad (2)$$

where $\rho_{\text{CO}_2+\text{SAC}}$ is the charge density of the $M_1/\text{Fe}_3\text{S}_4(111)$ SAC with the interacting CO₂ molecule, whereas ρ_{CO_2} and ρ_{SAC} are the charge densities of the adsorbate and catalyst surface with the same geometry as the adsorption mode.

We used the Visualization for Electronic and Structural Analysis (VESTA) program [239] to generate the structural representations and charge density flows. VASPKIT [240] was employed to extract and analyse the charge density differences and the projected den-

sity of states (PDOS). We used OriginPro [241] to plot the PDOS and energy diagrams.

3. Results and discussion

3.1. Pristine $\text{Fe}_3\text{S}_4(111)$ surface

Our starting point are the two non-polar stoichiometric and symmetric terminations of the pristine $\text{Fe}_3\text{S}_4(111)$ surface, where we have maintained the lattice parameters fixed at the value obtained for the bulk, illustrated in Fig. 1. The stacking sequences of the atomic planes are $\text{Fe}_{B3}\text{-S}_8\text{-Fe}_{A2}\text{-Fe}_{B2}\text{-Fe}_{A2}\text{-S}_8\text{-Fe}_{B6}\text{-S}_8\text{-Fe}_{A2}\text{-Fe}_{B2}\text{-Fe}_{A2}\text{-S}_8\text{-Fe}_{B3}$ and $\text{Fe}_B\text{-Fe}_{A2}\text{-S}_8\text{-Fe}_{B6}\text{-S}_8\text{-Fe}_{A2}\text{-Fe}_{B2}\text{-Fe}_{A2}\text{-S}_8\text{-Fe}_{B6}\text{-S}_8\text{-Fe}_{A2}\text{-Fe}_B$ for the terminations Fe_{B3} and Fe_B , respectively. We have used the $p(2 \times 1)$ surface unit cells to model terminations Fe_{B3} and Fe_B of the pristine $\text{Fe}_3\text{S}_4(111)$ facet, as these are the smallest periodically repeating simulation cells that allow the Tasker type 3 reconstructions [242] of the surface of this catalyst. The dipole moment was quenched before geometry optimisation of terminations Fe_{B3} and Fe_B by moving half of the cations from the exposed stoichiometric stacking sequence at the top of the surface to the bottom of the surface. Termination Fe_{B3} has a bulk-like structure consisting of a full monolayer (ML) of S atoms with a hexagonal cubic closed-packed (ccp) distribution, where 12.5% retain the tetrahedral configuration of the anions in the bulk, 62.5% become 3-fold and the remaining 25% have two dangling bonds. The topmost plane of termination Fe_{B3} also contains 0.375 ML of 3-fold Fe_B cations occupying the hexagonal close-packed (hcp) position, which are coordinated by the same central S atom. Termination Fe_B also comprises 1 ML of S atoms with the typical arrangement found in the bulk, where 37.5% have 4-fold configuration and the remaining 62.5% have one dangling bond. Termination Fe_B is decorated by 0.125 ML of 3-fold Fe_B ions in the hcp site and 0.25 ML of Fe_A ions with one dangling bond sited in the ccp position.

Fig. 2 displays the relaxations of the interplanar distances, which were estimated as $\Delta_{ij} = 100(d_{ij} - d_{ij}^0)/d_{ij}^0$, where d_{ij} is the distance between the relaxed i and $j = i + 1$ planes and d_{ij}^0 is the

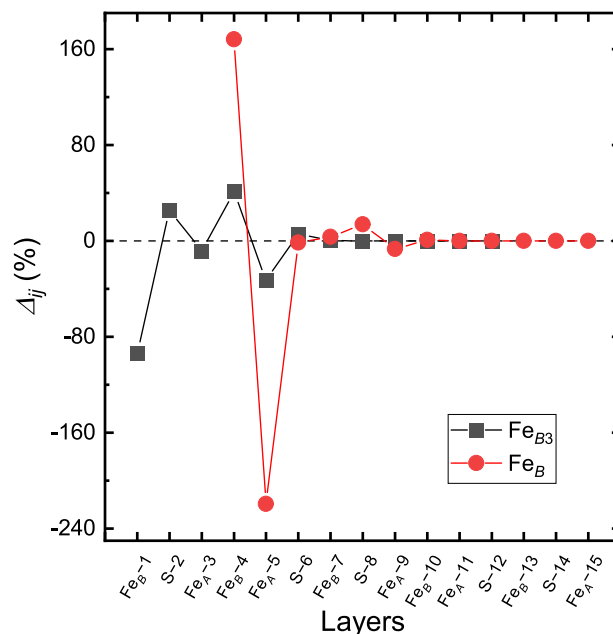


Fig. 2. Relaxation of the interplanar distances (Δ_{ij}) for the terminations (a) Fe_{B3} and (b) Fe_B of the $\text{Fe}_3\text{S}_4(111)$ surface in black and red, respectively. (For interpretation of the references to colour in this figure legend, the reader is referred to the web version of this article.)

distance between the corresponding layers in the bulk [243]. Our calculations suggest that the interplanar relaxation becomes progressively reduced towards the bulk after geometry optimisation for terminations Fe_{B3} and Fe_B . We found that consecutive i and j planes moved in opposite directions during the surface relaxations. The most exposed threefold cations of the Fe_{B-1} layer of termination Fe_{B3} experienced a strong relaxation towards the bulk of 93% when they merged with the subsurface S-2 layer, as shown in Fig. 1 (a) and 2. The sub-surface layer S-2 of soft anions, with negative charge and the ccp structure, suffered only a moderate 25% outward movement, as it had to accommodate the cations of the Fe_{B-1} layer. The shift of 8% towards the bulk of the sub-surface plane Fe_{A-3} can be justified as the electrostatic repulsion caused by the layer S-2 above, which lost part of its negative charge during the incorporation of the Fe_{B-1} layer. The sub-surface plane Fe_{B-4} moved outward by 41%, as it tried to merge with the plane Fe_{A-3} above. The positively charged Fe_{A-5} plane preferred to reduce by 33% its interplanar distance to the closer negatively charged S-6 layer, which in turn displaced outwards by 6%, due to their Coulomb attraction. The Fe_{B-7} plane, which was the last layer allowed to relax, only experienced a negligible shift towards the surface. The trend of the relaxation observed for termination Fe_B of the $\text{Fe}_3\text{S}_4(111)$ surface is in line with the relaxation calculated for the equivalent termination of the magnetite $\text{Fe}_3\text{O}_4(111)$ surface [224]. Moreover, the expansions and contractions of the interplanar distances Fe_{B-4} and Fe_{A-5} are considerably larger for termination Fe_B than for termination Fe_{B3} . Our calculations indicate that the Fe_{A-5} layer migrated by 219% to the sub-surface Fe_{B-7} plane, to reduce the number of dangling bonds, allowed by the soft nature of the anions within the intermediate S-6 layer, as illustrated in Fig. 2. Note that the Fe_{A-5} layer also migrates inwards in termination Fe_B of the $\text{Fe}_3\text{O}_4(111)$ surface, but it cannot diffuse across the O-6 layer, since the anions are hard and packed closer together in the oxide counterpart, whose lattice parameter is 1.5 Å smaller than in Fe_3S_4 [224]. The sub-surface Fe_{B-7} plane was displaced only by 3% towards the surface. Despite the negligible displacement of the S-6 plane, we found that the S-8 layer moved 14% outwards

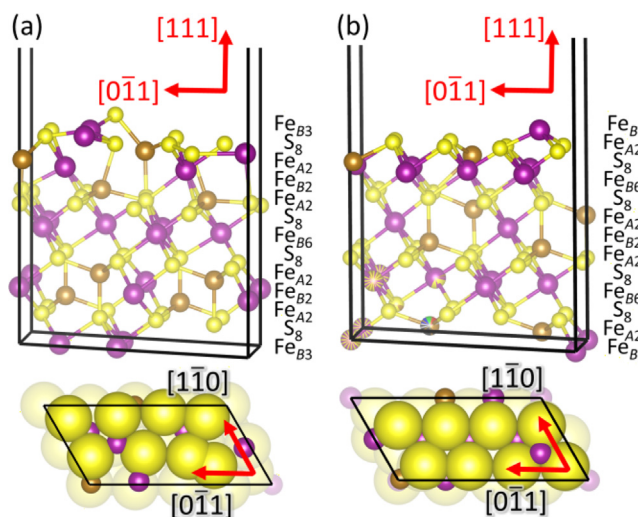


Fig. 1. Side (top panels) and top (bottom panels) views of terminations (a) Fe_{B3} and (b) Fe_B of the $\text{Fe}_3\text{S}_4(111)$ surface after geometry optimisation. Layers containing atoms with dangling bonds are highlighted. Crystallographic directions and stacking sequence of the atomic layers before geometry optimisation are indicated. Fe_A atoms are in dark yellow, Fe_B atoms are in magenta and S atoms are in light yellow. (For interpretation of the references to colour in this figure legend, the reader is referred to the web version of this article.)

due to the electrostatic attraction of the plane Fe_B -7 above containing more carriers of positive charge. The Fe_A -9 plane experienced only a minor shift towards the bulk.

The surface energies for the slab before (γ_u) and after relaxation (γ_r) were calculated as,

$$\gamma_u = \frac{E_{u,\text{Fe}_3\text{S}_4(111)} - n_b E_{\text{Fe}_3\text{S}_4}}{2A} \quad (3)$$

$$\gamma_r = \frac{E_{r,\text{Fe}_3\text{S}_4(111)} - n_b E_{\text{Fe}_3\text{S}_4}}{A} - \gamma_u \quad (4)$$

where $E_{u,\text{Fe}_3\text{S}_4}$, $E_{r,\text{Fe}_3\text{S}_4}$ and $E_{\text{Fe}_3\text{S}_4}$ are the energies of the unrelaxed $\text{Fe}_3\text{S}_4(111)$ surface slab, the half-relaxed slab and one Fe_3S_4 f.u. in the bulk, respectively, whereas A and n_b are the surface area and the number of Fe_3S_4 f.u. in the supercell, respectively. The degree of relaxation (R) was obtained as $R = 100(\gamma_u - \gamma_r)/\gamma_u$.

Our simulations suggest that termination Fe_B is the most stable of the $\text{Fe}_3\text{S}_4(111)$ planes, since it has the lowest surface energies before and after geometry optimisation, see Table 1. The relaxation of $R = 20.05\%$ calculated for termination Fe_B , which is the largest reported in this work, quantifies energetically the impact of the large displacement of the Fe_A -5 layer into the sub-surface Fe_B -7 layer. We have also obtained the Bader charges, which are lower for the atoms with dangling bonds than for the fully coordinated ions in the bulk, with the exception of the surface Fe_A cation in termination Fe_B , which has the same charge reported for the bulk [174]. In general, the ions of termination Fe_B are more ionic, *i.e.* have larger charge, than those in termination Fe_{B3} . The magnetic moments simulated for the exposed Fe_B and S atoms are larger in termination Fe_{B3} than in termination Fe_B . However, in both terminations our simulations only predict larger magnetic moments than in the bulk for the Fe_B ions with dangling bonds [174]. Both terminations display half-metallic properties, but Fe_{B3} has a band gap of 1.14 eV in the majority channel of spins, whereas termination Fe_B has a slightly larger energy gap of 1.28 eV in the minority spin channel. Note that the band gaps calculated for the $\text{Fe}_3\text{S}_4(111)$ surface are substantially lower than the value of ~ 2.8 eV obtained for the minority channel of the spins in the bulk [174]. The work function implies that termination Fe_B is slightly more reactive, by 0.137 eV, than termination Fe_{B3} , as it can supply more readily the electron from the Fermi level needed for the catalytic dissociation of CO_2 . In view of the above, we do not consider the Fe_{B3} termination for further analysis, due to its large relaxed surface energy, which makes it unlikely to be expressed in the crystal morphology of Fe_3S_4 .

Unsurprisingly, the possible terminations of the reconstructed Tasker type 3 (111) surface are similar for both Fe_3S_4 and its isostructural oxide counterpart magnetite Fe_3O_4 [224], which are spinel-structured materials. To rationalise the calculated proper-

ties of the most stable Fe_B termination of the $\text{Fe}_3\text{S}_4(111)$ surface, we compare it to the isostructural most stable termination of the $\text{Fe}_3\text{O}_4(111)$ surface. Despite having a similar stacking sequence, the $\text{Fe}_3\text{S}_4(111)$ surface has smaller unrelaxed and relaxed surface energies than the $\text{Fe}_3\text{O}_4(111)$ surface, with $\gamma_u = 98.59$ meV \AA^{-2} and $\gamma_r = 68.64$ meV \AA^{-2} , respectively [224]. Thus, replacing the soft S by the hard O atoms in the (111) surface increases the relaxation from 20.05% [224] to 30.4%. The average Bader charges of the undercoordinated Fe_A ions are 1.37 and 1.24 e atom $^{-1}$ in the (111) surface of the sulfide and oxide, respectively. However, we found the opposite trend in the Bader charges of the exposed Fe_B cations, with a lower value of 1.16 e atom $^{-1}$ computed for the $\text{Fe}_3\text{S}_4(111)$ surface and the larger $q = 1.21$ e atom $^{-1}$ for the $\text{Fe}_3\text{O}_4(111)$ surface. The average Bader charge of the S atoms with dangling bonds is -0.91 e atom $^{-1}$, whereas $q = -1.14$ e atom $^{-1}$ for O in the (111) surface, in agreement with the different electronegativities of the anions. Our simulations suggest that the difference in magnetic moments of the protruding Fe_A ions in the (111) surface is negligible between the sulfide and oxide phases, at 4.059 and 4.032 μ_B atom $^{-1}$, respectively. The magnetic moment of the exposed Fe_B ions is approximately 0.24 μ_B atom $^{-1}$ smaller in the $\text{Fe}_3\text{S}_4(111)$ surface than in the $\text{Fe}_3\text{O}_4(111)$ surface, at 3.91 μ_B atom $^{-1}$ calculated for the latter. The magnetic moment vanishes for the anions with dangling bonds in both the sulfide and oxide surfaces. A band gap of 1.28 and 0.69 eV in the minority spin channel was obtained for the Fe_3S_4 and $\text{Fe}_3\text{O}_4(111)$ surfaces [224], respectively, suggesting that the sulfide is a better insulator than the oxide. The larger work function of 5.658 eV calculated for the $\text{Fe}_3\text{S}_4(111)$ surface implies that this system is less reactive than the $\text{Fe}_3\text{O}_4(111)$ surface, with the smaller $\Phi = 3.90$ eV [220].

Weak electrostatic fields, typically of the order of 10^{-2} to 10^{-5} V \AA^{-1} , are only capable of orienting diatomic [244], linear [245] or asymmetric top polar molecules [246], depending on their dipole moment, rotational constant and rotational temperature, without affecting noticeably their electronic structure or geometry [177]. External electrostatic fields of intermediate strengths between 0.1 and 1.0 V \AA^{-1} are known to modify moderately the electronic structure of heterogeneous catalytic systems, affecting the energy of saddle points [176,247] and leading to new mechanistic pathways that are not available otherwise [177]. However, electrostatic fields with extreme strengths above 1 V \AA^{-1} can move considerably the atomic and molecular energy levels, leading to the desorption [221] and ionisation of molecules [248]. Since we want to model the effect of electrostatic fields in the dissociation of CO_2 using our SACs, we have decided to use strengths of $E = -0.475$ and 0.475 V \AA^{-1} . To gain further insight into termination Fe_B of the pristine $\text{Fe}_3\text{S}_4(111)$ surface, we have re-optimized its atomic positions under external electrostatic fields to simulate its structural, electronic and magnetic properties. Fig. 3 (a) displays the structure of the simulation slab, where we have indicated how we have applied the external electrostatic field $E = 0.475$ V \AA^{-1} by inserting a dipole sheet in the middle of the vacuum region between the surface and its periodically repeated image. The minima of the average electrostatic potential along the direction normal (R) to the simulation slab correspond to the position of the anion and the Fe_B layers, whereas the interlayer separation gaps lead to the local maxima, as shown in Fig. 3 (b). The slope of the average local potential in the vacuum region confirms that the slab is under the electrostatic field induced by the dipole sheet. $E_{\text{eff}} = 0.201$ V \AA^{-1} is the effective electric field between the two surfaces of the slab, which is calculated as the slope of the line linking the left high-potential side with the right low-potential side in the vacuum. The top of the highest occupied band, which is marked by the dashed line, lies below the lowest average electrostatic potential in the vacuum region, which confirms the absence of the unrealistic artificial field emission. The grey rectangle indicates

Table 1

Surface energies before (γ_u) and after relaxation (γ_r), percentage of relaxation (R), average atomic charges (q), average magnetic moments (m_s), energy gap (E_g) and work function (Φ) for terminations Fe_{B3} and Fe_B of the pristine $\text{Fe}_3\text{S}_4(111)$ surface. Negative atomic magnetic moments indicate antiparallel alignment.

Termination	Fe_{B3}	Fe_B
γ_u (meV \AA^{-2})	118.7	76.4
γ_r (meV \AA^{-2})	103.6	61.0
R (%)	12.72	20.05
$q(\text{Fe}_A)$ (e atom $^{-1}$)	1.246	1.372
$q(\text{Fe}_B)$ (e atom $^{-1}$)	1.126	1.162
$q(\text{S})$ (e atom $^{-1}$)	-0.792	-0.910
$m_s(\text{Fe}_A)$ (μ_B atom $^{-1}$)	3.963	4.059
$m_s(\text{Fe}_B)$ (μ_B atom $^{-1}$)	-3.793	-3.659
$m_s(\text{S})$ (μ_B atom $^{-1}$)	0.148	0.004
E_g (eV)	1.14	1.28
Φ (eV)	5.795	5.658

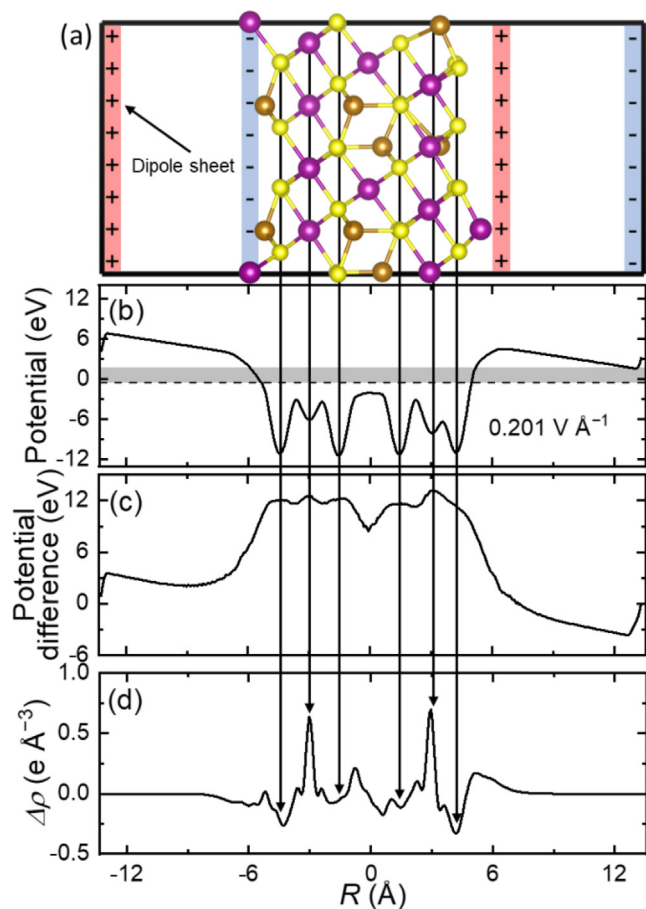


Fig. 3. (a) Structure of termination Fe_B of the pristine $\text{Fe}_3\text{S}_4(111)$ surface, (b) average electrostatic potential, (c) electrostatic potential difference and (c) charge density difference ($\Delta\rho$) along the direction normal (R) to the simulation slab. The electrostatic potential is plotted for the surface under an external electrostatic field of $E = 0.475 \text{ V } \text{\AA}^{-1}$, whereas the electrostatic potential difference and charge density difference ($\Delta\rho$) are represented for the slab under $E = 0.000$ and $0.475 \text{ V } \text{\AA}^{-1}$. The vertical arrows indicate the positions of the atomic layers in the slab. Fe_A atoms are in dark yellow, Fe_B atoms are in magenta and S atoms are in light yellow. (For interpretation of the references to colour in this figure legend, the reader is referred to the web version of this article.)

the maximum and minimum potential values used to calculate the work function of termination Fe_B of the pristine $\text{Fe}_3\text{S}_4(111)$ surface under an external electric field of $E = 0.475 \text{ V } \text{\AA}^{-1}$. It is clear from a theoretical point of view that the introduction of a planar dipole layer in the middle of the vacuum region parallel to the surface creates a potential jump that splits the work functions of the top and the bottom sides of the slab, as represented in Fig. 3 (a) and (b). To analyse the impact of the electrostatic fields on the electronic structure of termination Fe_B of the pristine $\text{Fe}_3\text{S}_4(111)$ surface, we have plotted the average electrostatic potential difference and the electronic charge density difference under an electrostatic field of $0.475 \text{ V } \text{\AA}^{-1}$ and under its absence, averaged in the direction parallel to the surface plane, with both surfaces having the same geometry as the system under the electrostatic field, see Fig. 3 (c) and (d). The potential difference shows that the electrostatic field is screened within the surface of our transition metal sulfide at roughly 12 eV, with a dip to 9 eV at the centre of the slab. The average potential difference decreases at the vacuum, which is a trend that continues on the relaxed side of the slab, explaining the reduction of the work function for positive external electrostatic fields. Moreover, there are charge oscillations within the slab of $\text{Fe}_3\text{S}_4(111)$, with large charge accumulations of around $0.6 \text{ e } \text{\AA}^{-3}$ on

the subsurface Fe_B layers and more modest charge depletions of $-0.25 \text{ e } \text{\AA}^{-3}$ on the exposed S layers. There is a small increase in charge of approximately $0.25 \text{ e } \text{\AA}^{-3}$ on the Fe_B cation with dangling bonds in the relaxed surface, which vanishes quickly at distances larger than 2.5 \AA away from the slab. In contrast, the average electrostatic potential difference remains constant at 0 eV within the slabs of the metallic Al(111) [221] and Pt(111) surface [249], decreasing and increasing on either side of the vacuum depending on the direction of the external electrostatic field. The charge density difference for these metallic systems also remains constant within the surface slab, with only large charge accumulation and depletion on the vacuum sides [221,249].

Fig. 4 (a), (c) and (d) illustrate that the electrostatic fields do not affect noticeably the relaxation pattern of the surface, nor the charges or magnetic moments of the Fe_A , Fe_B or S atoms, at least for the moderate strengths of up to $E = -0.475$ and $0.475 \text{ V } \text{\AA}^{-1}$ used in this study. Note that the small charge density differences of 0.25 and $-0.25 \text{ e } \text{\AA}^{-3}$ reported for the exposed Fe_B cation and S layer in Fig. 3 (d), become negligible when they are integrated within the atomic volume and divided by the number of the atoms in the layer. Thus, charges become relatively independent of the external electrostatic field strength. However, our calculations suggest that electrostatic fields, and particularly positive values,

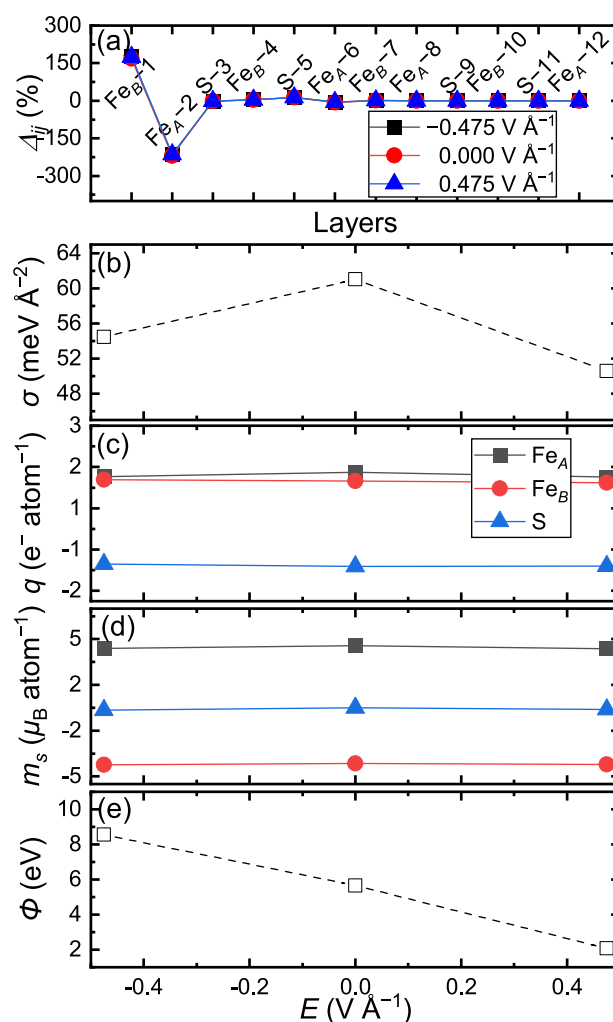
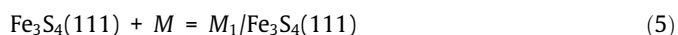


Fig. 4. (a) Relaxation of the interplanar distances (Δ_{ij}), (b) surface free energies (σ) at 0 K, (c) average atomic charges (q), (d) average atomic magnetic moments (m_s) and (e) work function (Φ) for termination Fe_B of the pristine $\text{Fe}_3\text{S}_4(111)$ surface in the absence and under external electrostatic fields $E = -0.475$ and $0.475 \text{ V } \text{\AA}^{-1}$.

stabilise thermodynamically the termination Fe_B of the pristine $\text{Fe}_3\text{S}_4(111)$ surface, as shown in Fig. 4 (b). The application of transverse electrostatic fields has a moderate effect on the band gap of termination Fe_B of the pristine $\text{Fe}_3\text{S}_4(111)$ surface, which reduces to 1.25 and 1.11 eV for $E = -0.475 \text{ V \AA}^{-1}$ and $E = 0.475 \text{ V \AA}^{-1}$, respectively. We also found that the work function has an inverse proportionality with the external electrostatic field, as $E = -0.475 \text{ V \AA}^{-1}$ leads to the most reactive surface with $\Phi = 2.086 \text{ eV}$, see Fig. 4 (e).

3.2. Single-atom catalysts

The incorporation of the single 3d transition metal atoms M and their impact on the geometries, electron charges and magnetic properties of termination Fe_B of the $\text{Fe}_3\text{S}_4(111)$ surface are discussed in this section. We have placed the single M atoms in the hcp position that was occupied in the bulk by the 0.125 ML of 3-fold Fe_B cations that were removed from the surface to eliminate the dipole moment of the simulation slab, as shown in Fig. 1 (b). The decoration of the $\text{Fe}_3\text{S}_4(111)$ surface using a single M_1 atom from groups III to XII of the periodic table was treated as a solid-state reaction and modelled according to,



where Sc, Ti, Co and Zn were simulated using the hcp primitive unit cell containing two atoms; V, Cr, Mn and Fe were modelled using the body-centred cubic (bcc) primitive cell comprising one atom; and Ni and Cu were calculated using the face-centred cubic (fcc) primitive cell consisting of one atom.

The surface free energy (σ) of the $M_1/\text{Fe}_3\text{S}_4(111)$ surface has been computed as,

$$\sigma = \gamma_r + \frac{E_{M_1/\text{Fe}_3\text{S}_4(111)} - E_{\text{Fe}_3\text{S}_4(111)} - E_M}{A} \quad (6)$$

where $E_{M_1/\text{Fe}_3\text{S}_4(111)}$ and E_M represent the energy of the $M_1/\text{Fe}_3\text{S}_4(111)$ catalyst and the energy of one atom in the bulk of M , respectively, in their thermodynamically most stable structures.

Fig. 5 (a) shows the distance between the single-atom M_1 and the S – 6 layer, which lie within the range 1.2 to 0.4 Å. Our calculations suggest that the interplanar separation becomes smaller as the external electrostatic field increases for $M = \text{Ti, V}$ and Cr , whereas Sc, Mn, Ni and Cu prefer to move away from the surface when $E = 0 \text{ V \AA}^{-1}$. We found that positive external electrostatic fields favour the displacement of Ti and Ni towards the sub-surface, as evidenced by the negative distance. Interestingly, the negative interplanar distance calculated for Fe in the absence of the external electrostatic field is in agreement with the embedding of the structural Fe_A cations observed in the pristine surface. The trend of the surface free energies at 0 K shows a general increase with the atomic number of M , see Fig. 5 (b). Positive external electrostatic fields are capable of stabilising thermodynamically the $M_1/\text{Fe}_3\text{S}_4(111)$ catalyst for $M = \text{Sc, Ti, V, Cr, Mn, Co}$ and Zn with respect to the $\text{Fe}_3\text{S}_4(111)$ surface. Our calculations suggest that removing the electrostatic field only marginally increases the surface free energy of these systems, with $\text{Zn}/\text{Fe}_3\text{S}_4(111)$ becoming the only catalyst less stable than the pristine $\text{Fe}_3\text{S}_4(111)$ surface. However, $\text{Sc}/\text{Fe}_3\text{S}_4(111)$ and $\text{Fe}/\text{Fe}_3\text{S}_4(111)$ are the only surfaces that are thermodynamically more stable than the parent structure under the negative electrostatic field $E = -0.475 \text{ V \AA}^{-1}$. The stability of $\text{Fe}/\text{Fe}_3\text{S}_4(111)$ SAC is barely affected by the external electrostatic field, while the systems containing Sc, Ni, Cu and Zn do not change their stabilities for $E = 0$ and $-0.475 \text{ V \AA}^{-1}$. Despite finding that external electrostatic fields can change the stability of the $M_1/\text{Fe}_3\text{S}_4(111)$ catalyst, understanding their impact on the bulk or surface atoms of the pure transition metals M is more complex. The free electrons of metals, which have a large conduction electron

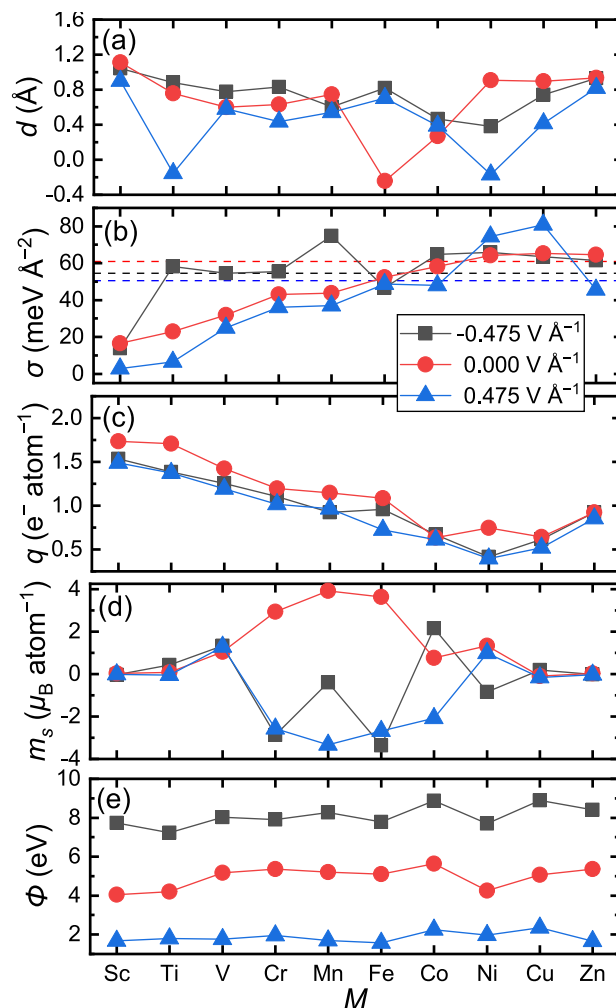


Fig. 5. (a) Interplanar distance (d) of M with respect to the S–6 layer, (b) surface free energies (σ) at 0 K, (c) atomic charges ($q(M)$), (d) atomic magnetic moments ($m_s(M)$) and (e) work function (Φ) for the $M_1/\text{Fe}_3\text{S}_4(111)$ catalyst in the absence and under external electrostatic fields $E = -0.475$ and 0.475 V \AA^{-1} . The dashed lines in (b) represent the surface energies (γ_r) of the pristine $\text{Fe}_3\text{S}_4(111)$ surface.

density [250], move within the bulk in the direction opposite to an external electrostatic field, creating an internal electric field of equal magnitude but with opposite direction to the external field. Thus, metal atoms within the bulk will not be under the influence of a net electrostatic field when an external electrostatic field is applied. For example, the local potential and charge does not change within the slab of the metallic $\text{Al}(111)$ [221] and $\text{Pt}(111)$ [249] surfaces after an external electrostatic field is applied. However, increasing changes in the potential are expected in the vacuum region as we move away from the surface of the slab and a sharp peak in the charge density difference is anticipated in the vacuum region close to the surface of the slab [221,249]. However, we cannot rule out that processes such as incorporation and sintering of the transition metal adatoms can take place, which is a common problem in SACs. Fig. 5 (c) shows that M becomes positively charged upon incorporation, which value decreases with atomic number from Sc to Ni, then increases again from the latter to Zn. Both positive and negative electrostatic fields reduce the charge of M with respect to $E = 0 \text{ V \AA}^{-1}$. The analysis of the magnetic moments suggests that Sc, Ti, Cu and Zn are non-magnetic, whereas V has a small value, see Fig. 5 (d). Cr, Mn, Fe, Co and Ni display magnetic moments, which change in direction but not in absolute value, when an external electrostatic field is applied. However, the

negative external electrostatic field has a more erratic effect on the magnetic moment of Mn and Co. Fig. 5 (e) illustrates that the work functions of the $M_1/\text{Fe}_3\text{S}_4(111)$ catalysts remain relatively constant for each external electrostatic field applied. Negative values of the external electrostatic field increase the work function of the SACs to around 8 eV, whereas $E = 0.475 \text{ V \AA}^{-1}$ enhances their catalytic activity by reducing the work function to approximately 2 eV.

In order to assess the nature of the interaction between the positively charged transition metal adatom and the surface of the catalyst, the electron density plot of the $\text{V}_1/\text{Fe}_3\text{S}_4(111)$ catalyst in the absence and in the presence of external electrostatic fields is shown in Fig. 6. We decided to construct contour plots in the plane parallel to the surface between the exposed S–6 layer and the nearest-neighbouring V and Fe atoms above. The plots show a denser mixture of charge density between the S and V atoms than between the S and Fe_B atoms, indicating a different degree of covalent bonding. We observe clearly that the electrons locate between the V adatom and the surrounding S atoms, forming covalent metal-support interactions (CMSI), which has also been found in a range of other types of SACs [251]. These covalent interactions, which are more pronounced in the absence of the external electrostatic field, were not detected for the interaction of the structural Fe_B cation and its surrounding S anions, which is essentially ionic.

3.3. CO_2 adsorption on $M_1/\text{Fe}_3\text{S}_4(111)$

Next, we have investigated the interaction of the single CO_2 molecule with the M_1 site of the $M_1/\text{Fe}_3\text{S}_4(111)$ catalysts. We have assessed the effect of these molecular adsorptions on the surface free energy, charge transfer, atomic magnetic moment and work function of the $M_1/\text{Fe}_3\text{S}_4(111)$ surfaces. We also discuss the geometries of the most favourable adsorption modes of the CO_2 molecule.

We have probed the adsorption of a single CO_2 molecule in a pre-activated configuration, where we reduced its point group from $D_{\infty h}$ to C_{2v} , by bending the apex angle to $\angle(\text{O}=\text{C}=\text{O}) = 130^\circ$. Note that this methodology, which we have applied in previous works, does not prevent the CO_2 molecule returning to the linear configuration if the adsorption site of the surface is unfavourable [166,167,200,220]. To characterise the adsorption configurations of our CO_2 molecule, we have borrowed the notation widely used in organometallics to describe the bonding and structural types of metal– CO_2 complexes, which is based on the hapticity of the ligand (μ_n) and the number of surface atoms (m) it can bridge (η^m)

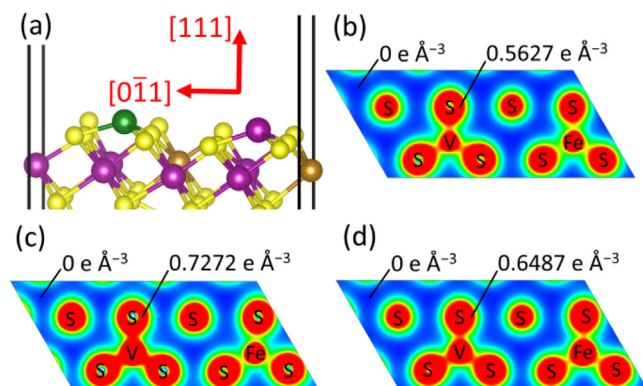


Fig. 6. (a) Side view of the $\text{V}_1/\text{Fe}_3\text{S}_4(111)$ surface for $E = 0 \text{ V \AA}^{-1}$. Crystallographic directions are indicated. V atom is in red, Fe_A atoms are in dark yellow, Fe_B atoms are in light yellow. Electron density plots of the $\text{V}_1/\text{Fe}_3\text{S}_4(111)$ surface for (b) $E = -0.475 \text{ V \AA}^{-1}$, (c) $E = 0 \text{ V \AA}^{-1}$ and (d) $E = 0.475 \text{ V \AA}^{-1}$ projected in the plane parallel to the surface between the exposed S–6 layer and the V atom. Minimum and maximum values for the electron density are indicated for each contour map. (For interpretation of the references to colour in this figure legend, the reader is referred to the web version of this article.)

[252–254]. We made the bent CO_2 molecule approach the surface in the $\mu_2 - \eta^2$ configuration, with both the C_2 rotational axis and the vertical mirror plane σ_v perpendicular to the surface, i.e. with the C atom coordinating one of the exposed S atoms of the catalyst and one of the molecular O atom binding the M_1 adatom. We placed the CO_2 molecule at 1.8 \AA from the surface of the catalyst before allowing the atomic positions of the interface to relax.

Our calculations indicate that the CO_2 molecule energetically prefers to interact molecularly with all the SACs investigated in this work, i.e. it does not dissociate spontaneously upon adsorption. Fig. 7 (a) shows that, as anticipated, the largest exothermic adsorption energies of CO_2 are calculated when a positive external electrostatic field is applied to the catalysts containing V, Cr, Mn, Ni and Cu. We obtained endothermic and therefore thermodynamically unfeasible adsorptions of the CO_2 molecule on $\text{Sc}_1/\text{Fe}_3\text{S}_4(111)$ under both positive and negative electrostatic fields; $\text{Cr}_1/\text{Fe}_3\text{S}_4(111)$ and $\text{Mn}_1/\text{Fe}_3\text{S}_4(111)$ at $E = -0.475 \text{ V \AA}^{-1}$; $\text{Fe}_1/\text{Fe}_3\text{S}_4(111)$ at $E = 0.475 \text{ V \AA}^{-1}$ and $\text{Ni}_1/\text{Fe}_3\text{S}_4(111)$ in the absence of an external electrostatic field. Interestingly, in the case of Ti, Co and Zn, negative external electrostatic fields led to the strongest adsorption modes for CO_2 on these SACs. The DFT simulations reveal that the $\text{Sc}_1/\text{Fe}_3\text{S}_4(111)$ surface only releases the largest adsorption energy in the series when $E = 0 \text{ V \AA}^{-1}$. Despite

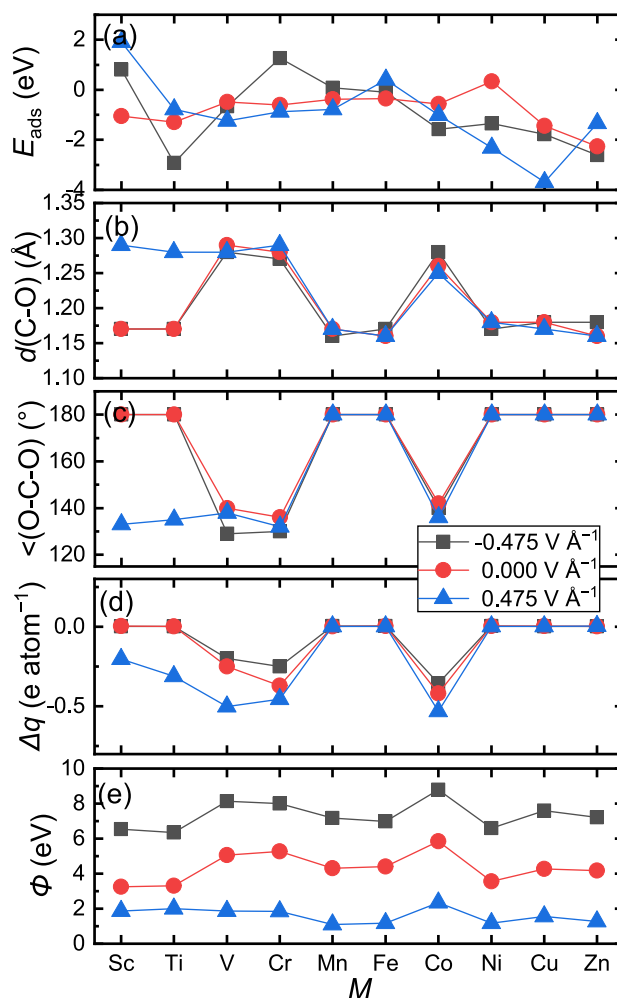


Fig. 7. (a) Adsorption energy (E_{ads}), (b) interatomic C–O distance (d), (c) O–C–O bond angle (\angle), (d) charge transfers (Δq) and (e) work function (Φ) for the interaction of CO_2 with the $M_1/\text{Fe}_3\text{S}_4(111)$ catalyst in the absence and under external electrostatic fields $E = -0.475$ and 0.475 V \AA^{-1} . Negative values of Δq indicate charge transfer from the surface to the adsorbate.

predicting exothermic adsorption modes for several of our SAC models, we found that the distance of the C–O bond is elongated only for $M = \text{Sc}$ and Ti under positive electrostatic fields, and for V , Cr and Co at any E value, see Fig. 7 (b). We have represented the adsorption modes of CO_2 on the $\text{Sc}_1/\text{Fe}_3\text{S}_4(111)$ catalyst in the absence and under negative and positive external electrostatic fields in Fig. 8 (a), (b) and (c). The CO_2 molecule showed a strong preference to adsorb in a linear configuration with the C–O bond distance relatively undisturbed when it interacts with the other less reactive SACs. The CO_2 molecule prefers to hover above the surface with the C atom lying at around 3.2–3.5 Å from the closest S anion and the O atom coordinating the Sc atom at 2.3 Å for $E = 0.000$ and $-0.475 \text{ V } \text{Å}^{-1}$, see Fig. 8 (a) and (b). However, positive potentials, which reduce the work function of the catalyst and make it easier to transfer charge to the antibonding molecular orbital of CO_2 , can also reinforce its chemical activation by favouring the creation of a bent geometry, with a dipole moment aligned in the same direction to the external electrostatic field, as represented in Fig. 7 (c). In contrast, the apex angle of the pre-activated CO_2 molecule also remains bent at any strength of the external electrostatic field, as a testament of chemical activation, when the adsorbate interacts with catalysts, such as $\text{V}_1/\text{Fe}_3\text{S}_4(111)$, that are capable of stretching the intramolecular bond distance, as shown in Fig. 7 (c) and Fig. 8 (d), (e) and (f). Previous work has shown that the CO_2 molecule prefers to adsorb linearly, releasing -0.02 eV on the Fe_A site of termination Fe_B of the pristine $\text{Fe}_3\text{S}_4(111)$ surface, which interaction is less thermodynamically feasible than on the exposed Fe_B site of the same termination, with an adsorption energy of -0.19 eV [255]. The simulations of several of our $M_1/\text{Fe}_3\text{S}_4(111)$ catalysts indicate a superior performance than the parent material, as even in the absence of an external electrostatic field, we predict larger adsorption energies and the activation of CO_2 with a bent molecular apex angle and elongated

interatomic C–O distances. The adsorbate gains the largest electronic charges when it coordinates the Sc-, Ti-, V-, Cr- and Co-based catalysts, especially under a positive external electrostatic field, see Fig. 7 (d). The values observed for the charge transfers are in agreement with the trend of the work function of the catalysts before interacting with the CO_2 molecule at $E = -0.475 \text{ V } \text{Å}^{-1}$. We have also quantified the work function of the catalyst surfaces after adsorption of a single CO_2 molecule, which indicates that despite these processes, the decreasing order of chemical reactivity remains $\Phi_{0.475 \text{ eV } \text{Å}^{-1}} < \Phi_{0 \text{ eV } \text{Å}^{-1}} < \Phi_{-0.475 \text{ eV } \text{Å}^{-1}}$, as shown in Fig. 7 (d).

3.4. CO_2 dissociation on $M_1/\text{Fe}_3\text{S}_4(111)$

We have also investigated the catalytic activity of our SAC models towards the dissociation of the CO_2 molecule, which is regarded as the initial step for the reduction and conversion of this greenhouse gas. Our dissociation mechanism involves breaking the C–O bond between the atoms that are interacting with the surface when the catalytic system is in the absence and under external electrostatic fields. In our dissociation pathways, the CO fragment remains bound to the surface S atom, whereas the O atom coordinates M_1 . We only discuss the dissociation process for the cases where the CO_2 molecule is chemically activated at the surface of our catalysts, i.e. where the apex angle is different from 180° .

We have considered that the initial states consist of the isolated SAC surfaces and the isolated CO_2 molecule, which energy has been calibrated to zero, to facilitate comparisons, see Fig. 9. For negative external electrostatic fields, only the catalytic systems containing V, Cr and Co are able to bend the apex angle of the adsorbed CO_2^* molecule, see Fig. 9 (a). The lowest activation energy of 1.8 eV for the three saddle points calculated under these conditions suggest that $\text{Co}_1/\text{Fe}_3\text{S}_4(111)$ is the best catalytic system, whereas

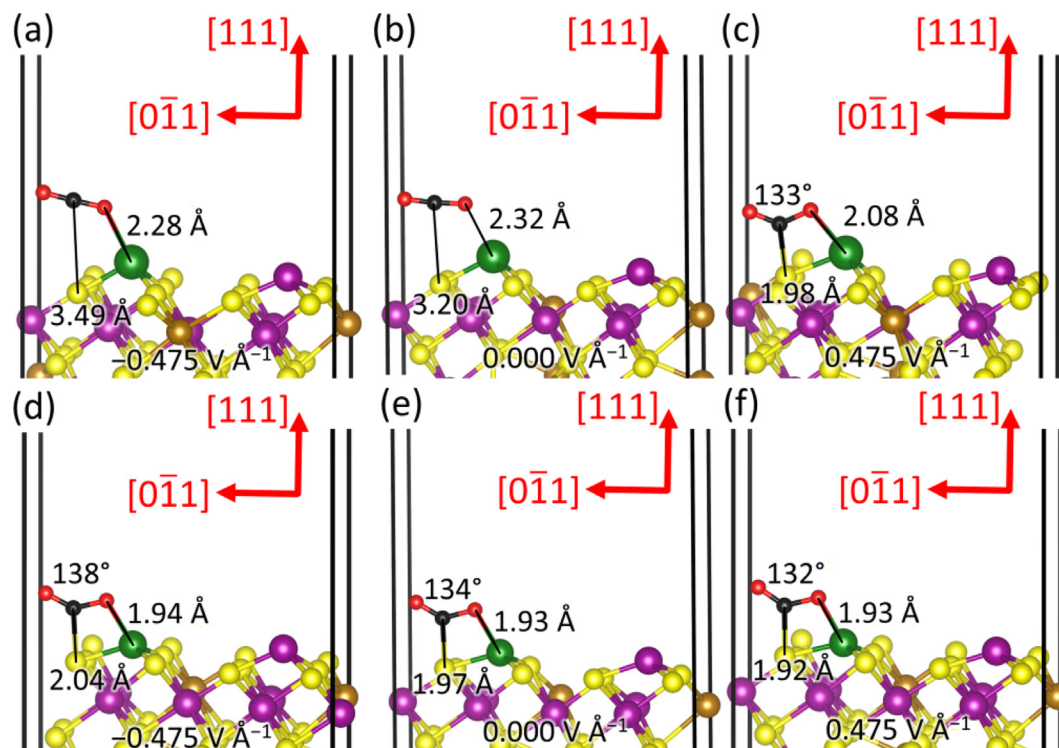


Fig. 8. Side view of the molecular adsorption of CO_2 on the surface of (a), (b) and (c) $\text{Sc}_1/\text{Fe}_3\text{S}_4(111)$ and (d), (e) and (f) $\text{V}_1/\text{Fe}_3\text{S}_4(111)$ in the absence and under external electrostatic fields. Interatomic distances, bond angles, crystallographic directions and the strength of the external electrostatic field are indicated. Sc and V atoms are in green, Fe_A atoms are in dark yellow, Fe_B atoms are in magenta, S atoms are in light yellow, O atoms are in red and C atoms are in black. (For interpretation of the references to colour in this figure legend, the reader is referred to the web version of this article.)

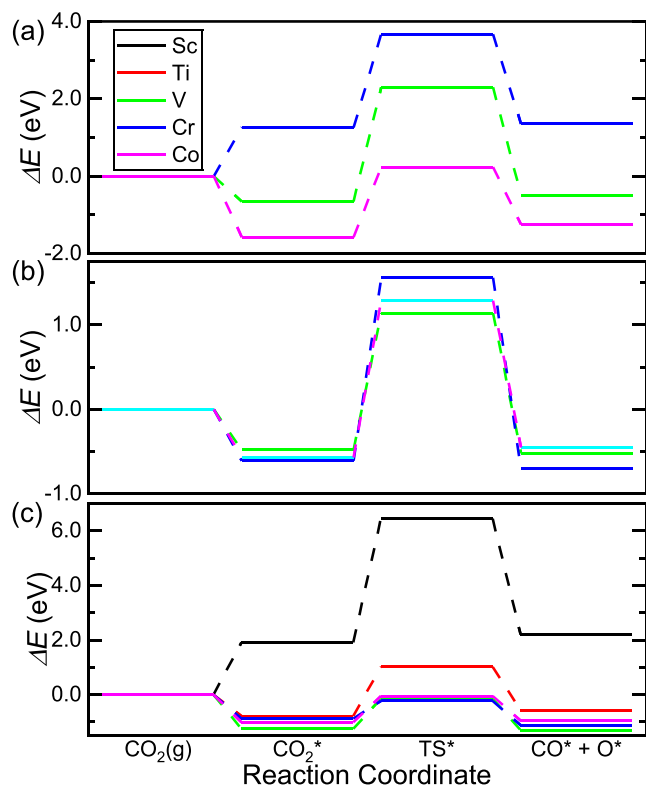


Fig. 9. Minimum energy pathways (MEPs) for the dissociation of CO_2 into CO and O on the $M_1/\text{Fe}_3\text{S}_4(111)$ surfaces at (a) $E = -0.475 \text{ V } \text{\AA}^{-1}$, (b) $E = 0.000 \text{ V } \text{\AA}^{-1}$ and (c) $E = 0.475 \text{ V } \text{\AA}^{-1}$. Minimum states and saddle point are represented by horizontal lines linked by dashed lines. Energies are referenced to the isolated CO_2 molecule and surface slab. Adsorbed species are presented followed by the symbol $*$.

the V-based SAC requires overcoming the largest energy barrier of 3.0 eV to dissociate the CO_2^* molecule. The final products are more stable than the isolated reactants when $M = \text{Co}$, but they are just less thermodynamically stable than the molecularly bound adsorbate, which implies that CO_2^* will prefer to stay in its molecular form at the surface of this SAC. In contrast, the CO^* and O^* fragments have very similar energies to the adsorbed CO_2^* molecule over the $\text{V}_1/\text{Fe}_3\text{S}_4(111)$ surface, but the large activation energy also suggests that the adsorbate will remain bound in undissociated form. The dissociation pathway for CO_2 over the Cr SAC shows that the molecule has a strong preference to stay in the gas phase, and thus adsorption and dissociation are unlikely processes.

In the absence of an external electrostatic field, we found that only the V-, Cr- and Co-based SACs are catalytically active, see Fig. 9 (b). Under these conditions, the CO_2 molecule forms stable chemisorption modes with the catalyst surfaces, but the activation energies of the saddle points are still larger than 1 eV for the three SACs. Despite displaying the largest energetic barrier for dissociation, the $\text{Cr}_1/\text{Fe}_3\text{S}_4(111)$ surface is the only SAC able to form dissociation products more stable than the molecularly adsorbed CO_2 . The most favourable mechanistic pathways for the dissociation of the CO_2 molecule were found when $M = \text{V}, \text{Cr}, \text{Co}$ and the external electrostatic field is $E = 0.475 \text{ V } \text{\AA}^{-1}$, see Fig. 9 (c). Under such electrostatic field and for these catalytic systems, the activation energy of the saddle points lies below the energy of the isolated surface and CO_2 molecule. Moreover, the energy of CO^* and O^* is only just below the energy level of the molecularly bound adsorbate for the V-, Cr- and Co-containing SACs, making these systems excellent catalysts for the dissociation of the CO_2 molecule. $\text{Sc}_1/\text{Fe}_3\text{S}_4(111)$ leads to a mechanistic pathway where reactant, transition state and final products have larger energies than the isolated CO_2 and

surface, whereas the transition state is 1.02 eV less stable than $\text{Ti}_1/\text{Fe}_3\text{S}_4(111)$ and the isolated CO_2 .

4. Conclusions

We have employed calculations based on the density functional theory to investigate the heterogeneous catalytic dissociation of CO_2 over the SACs $M_1/\text{Fe}_3\text{S}_4(111)$, where $M = \text{Sc}, \text{Ti}, \text{V}, \text{Cr}, \text{Mn}, \text{Fe}, \text{Co}, \text{Ni}, \text{Cu}, \text{Zn}$. We have simulated the pristine $\text{Fe}_3\text{S}_4(111)$ surface and determined the relaxation pattern of the atomic layers in the two possible reconstructed Tasker type 3 terminations. The protruding Fe_A cations in the termination with the lowest surface energy show a preference to migrate towards the sub-surface layer during optimisation. We predict that positive and negative electrostatic fields do not affect noticeably the relaxation pattern of the interplanar distances, atomic charges or atomic magnetic moments for the two terminations of the pristine $\text{Fe}_3\text{S}_4(111)$ surface.

However, external electrostatic fields will stabilise the most stable termination of the $\text{Fe}_3\text{S}_4(111)$ surface with respect to $E = 0 \text{ V } \text{\AA}^{-1}$, whereas only $E > 0$ can reduce the value of the work function. The incorporation of a single 3d transition metal adatom reduces the surface free energy at 0 K of the $M_1/\text{Fe}_3\text{S}_4(111)$ catalyst with respect to the pristine surface in the absence and for positive values of the external electrostatic field. Crucially, the work function, which we have used as a descriptor of the chemical reactivity of the SACs, remains below 2 eV for a positive external electrostatic field. The plot of the electron density for the $\text{V}_1/\text{Fe}_3\text{S}_4(111)$ catalyst at the three values of the electrostatic field considered in this work illustrates that there is a strong CMSI.

The adsorption energies of CO_2 on $M_1/\text{Fe}_3\text{S}_4(111)$ show a dependence on the nature of M and the external electrostatic field. The CO_2 molecule is only chemically activated for $M = \text{Sc}, \text{Ti}, \text{V}, \text{Cr}$ and Co , which is confirmed by the elongated C–O bond, the bent apex angle and the electron density charge gained by the adsorbate. The work function of the SACs under a positive external potential remains around 2 eV, even after adsorption of a CO_2 molecule, suggesting that the surface stays catalytically active. We have also investigated the minimum energy pathways for the dissociation of CO_2 on the $M_1/\text{Fe}_3\text{S}_4(111)$ surface under various external electrostatic field values. We found that the dissociation of the CO_2 molecule is only thermodynamically and kinetically feasible when $M = \text{V}, \text{Cr}$ or Co and the external electrostatic field is positive.

Future work will involve the simulation of SAC at the stepped surfaces of Fe_3S_4 , which contain a larger number of under-coordinated and more reactive atoms than the flat facets investigated in this study. Thermodynamically and kinetically achievable dissociation of CO_2 of SACs supported on Fe_3S_4 surfaces could lend further support to the iron-sulfur theory of the Origin of Life.

Data availability

All data created during this research are provided in full in the results section of this paper.

Declaration of Competing Interest

The authors declare that they have no known competing financial interests or personal relationships that could have appeared to influence the work reported in this paper.

Acknowledgements

Via our membership of the UK's HEC Materials Chemistry Consortium, which is funded by EPSRC (EP/R029431/1), this work used

the ARCHER2 UK National Supercomputing Service (<http://www.archer2.ac.uk>). We acknowledge the support of the Supercomputing Wales project, which is part-funded by the European Regional Development Fund (ERDF) via Welsh Government. This work was undertaken on ARC4, part of the High-Performance Computing facilities at the University of Leeds, United Kingdom. For the purpose of Open Access, the author has applied a CC BY public copyright licence to any Author Accepted Manuscript version arising from this submission.

Appendix A. Supplementary data

Supplementary data to this article can be found online at <https://doi.org/10.1016/j.jcat.2023.05.018>.

References

- H. Yang, L. Shang, Q. Zhang, R. Shi, G.I.N. Waterhouse, L. Gu, T. Zhang, A universal ligand mediated method for large scale synthesis of transition metal single atom catalysts, *Nat. Commun.* 10 (2019) 4585, <https://doi.org/10.1038/s41467-019-12510-0>.
- C. Xia, Y. Qiu, Y. Xia, P. Zhu, G. King, X. Zhang, Z. Wu, J.Y. Kim, D.A. Cullen, D. Zheng, P. Li, M. Shakouri, E. Heredia, P. Cui, H.N. Alshareef, Y. Hu, H. Wang, General synthesis of single-atom catalysts with high metal loading using graphene quantum dots, *Nat. Chem.* 13 (2021) 887–894, <https://doi.org/10.1038/s41557-021-00734-x>.
- B. Qiao, A. Wang, X. Yang, L.F. Allard, Z. Jiang, Y. Cui, J. Liu, J. Li, T. Zhang, Single-atom catalysis of CO oxidation using Pt₁/FeO_x, *Nat. Chem.* 3 (2011) 634–641, <https://doi.org/10.1038/nchem.1095>.
- Y. Shi, C. Zhao, H. Wei, J. Guo, S. Liang, A. Wang, T. Zhang, J. Liu, T. Ma, Single-atom catalysis in mesoporous photovoltaics: the principle of utility maximization, *Adv. Mater.* 26 (2014) 8147–8153, <https://doi.org/10.1002/adma.201402978>.
- L. Zhang, M. Zhou, A. Wang, T. Zhang, Selective hydrogenation over supported metal catalysts: from nanoparticles to single atoms, *Chem. Rev.* 120 (2020) 683–733, <https://doi.org/10.1021/acs.chemrev.9b00230>.
- Y. Wang, H. Su, Y. He, L. Li, S. Zhu, H. Shen, P. Xie, X. Fu, G. Zhou, C. Feng, D. Zhao, F. Xiao, X. Zhu, Y. Zeng, M. Shao, S. Chen, G. Wu, J. Zeng, C. Wang, Advanced electrocatalysts with single-metal-atom active sites, *Chem. Rev.* 120 (2020) 12217–12314, <https://doi.org/10.1021/acs.chemrev.0c00594>.
- C. Gao, J. Low, R. Long, T. Kong, J. Zhu, Y. Xiong, Heterogeneous single-atom photocatalysts: fundamentals and applications, *Chem. Rev.* 120 (2020) 12175–12216, https://doi.org/10.1021/ACS.CHEMREV.9B00840/ASSET/IMAGES/MEDIUM/CR9B00840_0048.GIF.
- R. Lang, X. Du, Y. Huang, X. Jiang, Q. Zhang, Y. Guo, K. Liu, B. Qiao, A. Wang, T. Zhang, Single-atom catalysts based on the metal-oxide interaction, *Chem. Rev.* 120 (2020) 11986–12043, https://doi.org/10.1021/ACS.CHEMREV.0C00797/ASSET/IMAGES/MEDIUM/CROC00797_0050.GIF.
- H.Y. Zhuo, X. Zhang, J.X. Liang, Q. Yu, H. Xiao, J. Li, Theoretical understandings of graphene-based metal single-atom catalysts: stability and catalytic performance, *Chem. Rev.* 120 (2020) 12315–12341, https://doi.org/10.1021/ACS.CHEMREV.0C00818/ASSET/IMAGES/MEDIUM/CROC00818_0017.GIF.
- K.T. Rim, D. Eom, L. Liu, E. Stolyarova, J.M. Raitano, S.-W. Chan, M. Flytzani-Stephanopoulos, G.W. Flynn, Charging and chemical reactivity of gold nanoparticles and adatoms on the (111) surface of single-crystal magnetite: a scanning tunneling microscopy/spectroscopy study, *J. Phys. Chem. C* 113 (2009) 10198–10205, <https://doi.org/10.1021/jp8112599>.
- R. Bliem, R. Kosak, L. Perneckzy, Z. Novotny, O. Gamba, D. Fobes, Z. Mao, M. Schmid, P. Blaha, U. Diebold, G.S. Parkinson, Cluster nucleation and growth from a highly supersaturated adatom phase: silver on magnetite, *ACS Nano*. 8 (2014) 7531–7537, <https://doi.org/10.1021/nn502895s>.
- Z. Novotny, G. Argentero, Z. Wang, M. Schmid, U. Diebold, G.S. Parkinson, Ordered array of single adatoms with remarkable thermal stability: Au/Fe₃O₄, *Phys. Rev. Lett.* 108 (2012), <https://doi.org/10.1103/PhysRevLett.108.216103>.
- K.T. Rim, D. Eom, S.-W. Chan, M. Flytzani-Stephanopoulos, G.W. Flynn, X.-D. Wen, E.R. Batista, Scanning tunneling microscopy and theoretical study of water adsorption on Fe₃O₄: implications for catalysis, *J. Am. Chem. Soc.* 134 (2012) 18979–18985, <https://doi.org/10.1021/ja305294x>.
- R. Bliem, J. van der Hoeven, A. Zavodny, O. Gamba, J. Pavelec, P.E. de Jongh, M. Schmid, U. Diebold, G.S. Parkinson, An atomic-scale view of CO and H₂ oxidation on a Pt/Fe₃O₄ model catalyst, *Angew. Chem. Int. Ed.* 54 (2015) 13999–14002, <https://doi.org/10.1002/anie.201507368>.
- M.D. Marcinkowski, S.F. Yuk, N. Doudin, R.S. Smith, M.-T. Nguyen, B.D. Kay, V.-A. Glezakou, R. Rousseau, Z. Dohnalek, Low-temperature oxidation of methanol to formaldehyde on a model single-atom catalyst: Pd atoms on Fe₃O₄(001), *ACS Catal.* 9 (2019) 10977–10982, <https://doi.org/10.1021/acscatal.9b03891>.
- R. Bliem, J.E.S. van der Hoeven, J. Hulva, J. Pavelec, O. Gamba, P.E. de Jongh, M. Schmid, P. Blaha, U. Diebold, G.S. Parkinson, Dual role of CO in the stability of subnano Pt clusters at the Fe₃O₄(001) surface, *Proc. Natl. Acad. Sci. U.S.A.* 113 (32) (2016) 8921–8926, <https://doi.org/10.1073/pnas.1605649113>.
- G.S. Parkinson, Z. Novotny, G. Argentero, M. Schmid, J. Pavelec, R. Kosak, P. Blaha, U. Diebold, Carbon monoxide-induced adatom sintering in a Pd-Fe₃O₄ model catalyst, *Nat. Mater.* 12 (2013) 724–728, <https://doi.org/10.1038/nmat3667>.
- R. Lang, W. Xi, J.-C. Liu, Y.-T. Cui, T. Li, A.F. Lee, F. Chen, Y. Chen, L. Li, L. Li, J. Lin, S. Miao, X. Liu, A.-Q. Wang, X. Wang, J. Luo, B. Qiao, J. Li, T. Zhang, Non defect-stabilized thermally stable single-atom catalyst, *Nat. Commun.* 10 (2019) 234, <https://doi.org/10.1038/s41467-018-08136-3>.
- W. Qu, X. Liu, J. Chen, Y. Dong, X. Tang, Y. Chen, Single-atom catalysts reveal the dinuclear characteristic of active sites in NO selective reduction with NH₃, *Nat. Commun.* 11 (2020) 1532, <https://doi.org/10.1038/s41467-020-15261-5>.
- J. Lin, A. Wang, B. Qiao, X. Liu, X. Yang, X. Wang, J. Liang, J. Li, J. Liu, T. Zhang, Remarkable performance of Ir₁/FeO_x single-atom catalyst in water gas shift reaction, *J. Am. Chem. Soc.* 135 (2013) 15314–15317, <https://doi.org/10.1021/ja408574m>.
- B. Qiao, J.-X. Liang, A. Wang, C.-Q. Xu, J. Li, T. Zhang, J.J. Liu, Ultrastable single-atom gold catalysts with strong covalent metal-support interaction (CMSI), *Nano Res.* 8 (2015) 2913–2924, <https://doi.org/10.1007/s12274-015-0796-9>.
- X. Sun, J. Lin, Y. Zhou, L. Li, Y. Su, X. Wang, T. Zhang, FeO_x supported single-atom Pd bifunctional catalyst for water gas shift reaction, *AIChE J.* 63 (2017) 4022–4031, <https://doi.org/10.1002/aic.15759>.
- Y. Chen, J. Lin, L. Li, B. Qiao, J. Liu, Y. Su, X. Wang, Identifying size effects of Pt as single atoms and nanoparticles supported on FeO_x for the water-gas shift reaction, *ACS Catal.* 8 (2018) 859–868, <https://doi.org/10.1021/acscatal.7b02751>.
- J. Lin, B. Qiao, N. Li, L. Li, X. Sun, J. Liu, X. Wang, T. Zhang, Little do more: a highly effective Pt₁/FeO_x single-atom catalyst for the reduction of NO by H₂, *Chem. Commun.* 51 (2015) 7911–7914, <https://doi.org/10.1039/C5CC00714C>.
- J. Jones, H. Xiong, A.T. DeLaRiva, E.J. Peterson, H. Pham, S.R. Challa, G. Qi, S. Oh, M.H. Wiebenga, X.I. Pereira Hernández, Y. Wang, A.K. Datye, Thermally stable single-atom platinum-on-ceria catalysts via atom trapping, *Science* 353 (2016) 150–154, <https://doi.org/10.1126/science.aaf8800>.
- D. Kunwar, S. Zhou, A. DeLaRiva, E.J. Peterson, H. Xiong, X.I. Pereira-Hernández, S.C. Purdy, R. ter Veen, H.H. Brongersma, J.T. Miller, H. Hashiguchi, L. Kovarik, S. Lin, H. Guo, Y. Wang, A.K. Datye, Stabilizing high metal loadings of thermally stable platinum single atoms on an industrial catalyst support, *ACS Catal.* 9 (2019) 3978–3990, <https://doi.org/10.1021/acscatal.8b04885>.
- Y.-G. Wang, D. Mei, V.-A. Glezakou, J. Li, R. Rousseau, Dynamic formation of single-atom catalytic active sites on ceria-supported gold nanoparticles, *Nat. Commun.* 6 (2015) 6511, <https://doi.org/10.1038/ncomms7511>.
- W. Song, E.J.M. Hensen, mechanistic aspects of the water-gas shift reaction on isolated and clustered Au atoms on CeO₂(110): a density functional theory study, *ACS Catal.* 4 (2014) 1885–1892, <https://doi.org/10.1021/cs401206e>.
- B. Qiao, J. Liu, Y.-G. Wang, Q. Lin, X. Liu, A. Wang, J. Li, T. Zhang, J. (Jimmy) Liu, Highly efficient catalysis of preferential oxidation of CO in H₂-rich stream by gold single-atom catalysts, *ACS Catal.* 5 (2015) 6249–6254, <https://doi.org/10.1021/acscatal.5b01114>.
- T. Li, F. Liu, Y. Tang, L. Li, S. Miao, Y. Su, J. Zhang, J. Huang, H. Sun, M. Haruta, A. Wang, B. Qiao, J. Li, T. Zhang, Maximizing the number of interfacial sites in single-atom catalysts for the highly selective, solvent-free oxidation of primary alcohols, *Angew. Chem.* 130 (2018) 7921–7925, <https://doi.org/10.1002/ange.201803272>.
- Y. Chen, J. Gao, Z. Huang, M. Zhou, J. Chen, C. Li, Z. Ma, J. Chen, X. Tang, Sodium rivals silver as single-atom active centers for catalyzing abatement of formaldehyde, *Environ. Sci. Technol.* 51 (2017) 7084–7090, <https://doi.org/10.1021/acs.est.7b00499>.
- Y. Chen, T. Kasama, Z. Huang, P. Hu, J. Chen, X. Liu, X. Tang, Highly dense isolated metal atom catalytic sites: dynamic formation and in situ observations, *Chem. – A Eur. J.* 21 (2015) 17397–17402, <https://doi.org/10.1002/chem.201503068>.
- S. Ni, H. Zhang, Y. Zhao, X. Li, Y. Sun, J. Qian, Q. Xu, P. Gao, D. Wu, K. Kato, M. Yamauchi, Y. Sun, Single atomic Ag enhances the bifunctional activity and cycling stability of MnO₂, *Chem. Eng. J.* 366 (2019) 631–638, <https://doi.org/10.1016/j.cej.2019.02.084>.
- F. Xu, Z. Huang, P. Hu, Y. Chen, L. Zheng, J. Gao, X. Tang, The promotion effect of isolated potassium atoms with hybridized orbitals in catalytic oxidation, *Chem. Commun.* 51 (2015) 9888–9891, <https://doi.org/10.1039/C5CC02476E>.
- Z. Huang, X. Gu, Q. Cao, P. Hu, J. Hao, J. Li, X. Tang, Catalytically active single-atom sites fabricated from silver particles, *Angew. Chem. Int. Ed.* 51 (2012) 4198–4203, <https://doi.org/10.1002/anie.201109065>.
- P. Hu, Z. Huang, Z. Amghouz, M. Makkee, F. Xu, F. Kapteijn, A. Dikhtiarenko, Y. Chen, X. Gu, X. Tang, Electronic metal-support interactions in single-atom catalysts, *Angew. Chem. Int. Ed.* 53 (2014) 3418–3421, <https://doi.org/10.1002/anie.201309248>.
- L. Wang, W. Zhang, S. Wang, Z. Gao, Z. Luo, X. Wang, R. Zeng, A. Li, H. Li, M. Wang, X. Zheng, J. Zhu, W. Zhang, C. Ma, R. Si, J. Zeng, Atomic-level insights in optimizing reaction paths for hydroformylation reaction over Rh/CoO single-atom catalyst, *Nat. Commun.* 7 (2016) 14036, <https://doi.org/10.1038/ncomms14036>.
- S. Zhang, J.-J. Shan, Y. Zhu, A.I. Frenkel, A. Patlolla, W. Huang, S.J. Yoon, L. Wang, H. Yoshida, S. Takeda, F. (Feng) Tao, WGS catalysis and in situ studies of CoO_{1-x}, PtCo_n/Co₃O₄, and Pt_mCo_n/CoO_{1-x} nanorod catalysts, *J. Am. Chem. Soc.* 135 (22) (2013) 8283–8293, <https://doi.org/10.1021/ja401967y>.
- L. Wang, S. Zhang, Y. Zhu, A. Patlolla, J. Shan, H. Yoshida, S. Takeda, A.I. Frenkel, F. (Feng) Tao, Catalysis and in situ studies of Rh₁/Co₃O₄ nanorods in

- reduction of NO with H₂, ACS Catal. 3 (5) (2013) 1011–1019, <https://doi.org/10.1021/cs300816u>.
- [40] L. Nguyen, S. Zhang, L. Wang, Y. Li, H. Yoshida, A. Patlolla, S. Takeda, A.I. Frenkel, F. (Feng) Tao, Reduction of nitric oxide with hydrogen on catalysts of singly dispersed bimetallic sites Pt₁Co_m and Pd₁Co_m, ACS Catal. 6 (2) (2016) 840–850, <https://doi.org/10.1021/acscatal.5b00842>.
- [41] S. Zhang, L. Nguyen, J.-X. Liang, J. Shan, J. Liu, A.I. Frenkel, A. Patlolla, W. Huang, J. Li, F. Tao, Catalysis on singly dispersed bimetallic sites, Nat. Commun. 6 (2015) 7938, <https://doi.org/10.1038/ncomms8938>.
- [42] Y. Lou, Y. Cai, W. Hu, L. Wang, Q. Dai, W. Zhan, Y. Guo, P. Hu, X.-M. Cao, J. Liu, Y. Guo, Identification of Active area as active center for CO oxidation over single Au atom catalyst, ACS Catal. 10 (2020) 6094–6101, <https://doi.org/10.1021/acscatal.0c01303>.
- [43] B. Qiao, J. Lin, A. Wang, Y. Chen, T. Zhang, J. Liu, Highly active Au₁/Co₃O₄ single-atom catalyst for CO oxidation at room temperature, Chin. J. Catal. 36 (2015) 1505–1511, [https://doi.org/10.1016/S1872-2067\(15\)60889-0](https://doi.org/10.1016/S1872-2067(15)60889-0).
- [44] Q. Wang, X. Huang, Z.L. Zhao, M. Wang, B. Xiang, J. Li, Z. Feng, H. Xu, M. Gu, Ultrahigh-loading of Ir single atoms on NiO matrix to dramatically enhance oxygen evolution reaction, J. Am. Chem. Soc. 142 (2020) 7425–7433, https://doi.org/10.1021/JACS.9B12642/ASSET/IMAGES/LARGE/JA9B12642_0005.JPEG.
- [45] X. Zhou, W. Yang, Q. Chen, Z. Geng, X. Shao, J. Li, Y. Wang, D. Dai, W. Chen, G. Xu, X. Yang, K. Wu, Stable Pt single atoms and nanoclusters on ultrathin CuO film and their performances in CO oxidation, J. Phys. Chem. C 120 (2016) 1709–1715, <https://doi.org/10.1021/acs.jpcc.5b11362>.
- [46] X. Zhou, Q. Shen, K. Yuan, W. Yang, Q. Chen, Z. Geng, J. Zhang, X. Shao, W. Chen, G. Xu, X. Yang, K. Wu, Unraveling charge state of supported Au single-atoms during CO oxidation, J. Am. Chem. Soc. 140 (2018) 554–557, <https://doi.org/10.1021/jacs.7b10394>.
- [47] A.J. Therrien, A.J.R. Hensley, M.D. Marcinkowski, R. Zhang, F.R. Lucci, B. Coughlin, A.C. Schilling, J.-S. McEwen, E.C.H. Sykes, An atomic-scale view of single-site Pt catalysis for low-temperature CO oxidation, Nat. Catal. 1 (2018) 192–198, <https://doi.org/10.1038/s41929-018-0028-2>.
- [48] B. Han, R. Lang, H. Tang, J. Xu, X.-K. Gu, B. Qiao, J. Liu, Superior activity of Rh₁/ZnO single-atom catalyst for CO oxidation, Chin. J. Catal. 40 (2019) 1847–1853, [https://doi.org/10.1016/S1872-2067\(19\)63411-X](https://doi.org/10.1016/S1872-2067(19)63411-X).
- [49] F. Chen, X. Jiang, L. Zhang, R. Lang, B. Qiao, Single-atom catalysis: Bridging the homo- and heterogeneous catalysis, Chin. J. Catal. 39 (2018) 893–898, [https://doi.org/10.1016/S1872-2067\(18\)63047-5](https://doi.org/10.1016/S1872-2067(18)63047-5).
- [50] H. Zhou, X. Yang, A. Wang, S. Miao, X. Liu, X. Pan, Y. Su, L. Li, Y. Tan, T. Zhang, Pd/ZnO catalysts with different origins for high chemoselectivity in acetylene semi-hydrogenation, Chin. J. Catal. 37 (2016) 692–699, [https://doi.org/10.1016/S1872-2067\(15\)61090-7](https://doi.org/10.1016/S1872-2067(15)61090-7).
- [51] R. Lang, T. Li, D. Matsumura, S. Miao, Y. Ren, Y.-T. Cui, Y. Tan, B. Qiao, L. Li, A. Wang, X. Wang, T. Zhang, Hydroformylation of olefins by a rhodium single-atom catalyst with activity comparable to RhCl(PPh₃)₃, Angew. Chem. 128 (2016) 16288–16292, <https://doi.org/10.1002/ange.201607885>.
- [52] H. Zhou, X. Yang, L. Li, X. Liu, Y. Huang, X. Pan, A. Wang, J. Li, T. Zhang, PdZn intermetallic nanostructure with Pd–Zn–Pd ensembles for highly active and chemoselective semi-hydrogenation of acetylene, ACS Catal. 6 (2016) 1054–1061, <https://doi.org/10.1021/acscatal.5b01933>.
- [53] T. Wu, X. Zhu, Z. Xing, S. Mou, C. Li, Y. Qiao, Q. Liu, Y. Luo, X. Shi, Y. Zhang, X. Sun, Greatly improving electrochemical N₂ reduction over TiO₂ nanoparticles by iron doping, Angew. Chem. 131 (2019) 18620–18624, <https://doi.org/10.1002/ange.201911153>.
- [54] G. Shen, R. Zhang, L. Pan, F. Hou, Y. Zhao, Z. Shen, W. Mi, C. Shi, Q. Wang, X. Zhang, J. Zou, Regulating the spin state of Fe^{III} by atomically anchoring on ultrathin titanium dioxide for efficient oxygen evolution electrocatalysis, Angew. Chem. 132 (2020) 2333–2337, <https://doi.org/10.1002/ange.201913080>.
- [55] Q. Shen, C. Cao, R. Huang, L. Zhu, X. Zhou, Q. Zhang, L. Gu, W. Song, Single chromium atoms supported on titanium dioxide nanoparticles for synergistic catalytic methane conversion under mild conditions, Angew. Chem. 132 (2020) 1232–1235, <https://doi.org/10.1002/ange.201913309>.
- [56] S. Koust, L. Arnarson, P.G. Moses, Z. Li, I. Beinik, J.V. Lauritsen, S. Wendt, Facile embedding of single vanadium atoms at the anatase TiO₂(101) surface, Phys. Chem. Chem. Phys. 19 (14) (2017) 9424–9431, <https://doi.org/10.1039/C6CP06965G>.
- [57] M. Yang, L.F. Allard, M. Flytzani-Stephanopoulos, Atomically dispersed Au(OH)_x species bound on titania catalyze the low-temperature water–gas shift reaction, J. Am. Chem. Soc. 135 (2013) 3768–3771, <https://doi.org/10.1021/ja312646d>.
- [58] K. Asakura, H. Nagahiro, N. Ichikuni, Y. Iwasawa, Structure and catalytic combustion activity of atomically dispersed Pt species at MgO surface, Appl. Catal. A Gen. 188 (1999) 313–324, [https://doi.org/10.1016/S0926-860X\(99\)00247-1](https://doi.org/10.1016/S0926-860X(99)00247-1).
- [59] S. Abbet, U. Heiz, H. Häkkinen, U. Landman, CO oxidation on a single Pd atom supported on magnesia, Phys. Rev. Lett. 86 (2001) 5950–5953, <https://doi.org/10.1103/PhysRevLett.86.5950>.
- [60] S. Abbet, A. Sanchez, U. Heiz, W.-D. Schneider, A.M. Ferrari, G. Pacchioni, N. Rösch, acetylene cyclotrimerization on supported size-selected Pd_n clusters (1 ≤ n ≤ 30): one atom is enough!, J. Am. Chem. Soc. 122 (2000) 3453–3457, <https://doi.org/10.1021/ja9922476>.
- [61] A. Uzun, V. Ortolan, N.D. Browning, B.C. Gates, Site-isolated iridium complexes on MgO powder: individual Ir atoms imaged by scanning transmission electron microscopy, Chem. Commun. (2009) 4657, <https://doi.org/10.1039/b823171k>.
- [62] A. Uzun, V. Ortolan, N.D. Browning, B.C. Gates, A site-isolated mononuclear iridium complex catalyst supported on MgO: characterization by spectroscopy and aberration-corrected scanning transmission electron microscopy, J. Catal. 269 (2010) 318–328, <https://doi.org/10.1016/j.jcat.2009.11.017>.
- [63] E.J. Peterson, A.T. DeLaRiva, S. Lin, R.S. Johnson, H. Guo, J.T. Miller, J.H. Kwak, C.H.F. Peden, B. Kiefer, L.F. Allard, F.H. Ribeiro, A.K. Datye, Low-temperature carbon monoxide oxidation catalysed by regenerable atomically dispersed palladium on alumina, Nat. Commun. 5 (2014) 1–11, <https://doi.org/10.1038/ncomms5885>.
- [64] A. Liu, L. Liu, Y. Cao, J. Wang, R. Si, F. Gao, L. Dong, Controlling dynamic structural transformation of atomically dispersed CuO_x species and influence on their catalytic performances, ACS Catal. 9 (2019) 9840–9851, <https://doi.org/10.1021/acscatal.9b02773>.
- [65] S.F.J. Hackett, R.M. Brydson, M.H. Gass, I. Harvey, A.D. Newman, K. Wilson, A.F. Lee, High-activity, single-site mesoporous Pd/Al₂O₃ catalysts for selective aerobic oxidation of allylic alcohols, Angew. Chem. Int. Ed. 46 (2007) 8593–8596, <https://doi.org/10.1002/anie.200702534>.
- [66] E.A. Vovchko, J.T. Yates, Activation of O₂ on a photochemically generated Rh^I site on an Al₂O₃ surface: low-temperature O₂ dissociation and CO oxidation, J. Am. Chem. Soc. 120 (1998) 10523–10527, <https://doi.org/10.1021/ja981241y>.
- [67] K. Asakura, W.J. Chun, M. Shirai, K. Tomishige, Y. Iwasawa, In-situ polarization-dependent total-reflection fluorescence XAFS studies on the structure transformation of Pt clusters on α -Al₂O₃(0001), J. Phys. Chem. B 101 (1997) 5549–5556, <https://doi.org/10.1021/jp970394p>.
- [68] Y. Zhai, D. Pierre, R. Si, W. Deng, P. Ferrin, A.U. Nilekar, G. Peng, J.A. Herron, D. C. Bell, H. Saltsburg, M. Mavrikakis, M. Flytzani-Stephanopoulos, Alkali-stabilized Pt-OH_x species catalyze low-temperature water–gas shift reactions, Science 329 (2010) 1633–1636, <https://doi.org/10.1126/science.1192449>.
- [69] L.M. Azofra, N. Morlanés, A. Poater, M.K. Samantary, B. Vidjayacoumar, K. Albahily, L. Cavallo, J.-M. Basset, Single-site molybdenum on solid support materials for catalytic hydrogenation of N₂-into-NH₃, Angew. Chem. 130 (2018) 16038–16042, <https://doi.org/10.1002/ange.201810409>.
- [70] P.T. Tanev, M. Chibwe, T.J. Pinnavaia, Titanium-containing mesoporous molecular sieves for catalytic oxidation of aromatic compounds, Nature 368 (1994) 321–323, <https://doi.org/10.1038/368321a0>.
- [71] J. Qi, J. Finzel, H. Robotzaji, M. Xu, A.S. Hoffman, S.R. Bare, X. Pan, P. Christopher, Selective methanol carbonylation to acetic acid on heterogeneous atomically dispersed ReO₄/SiO₂ catalysts, J. Am. Chem. Soc. 142 (2020) 14178–14189, <https://doi.org/10.1021/jacs.0c05026>.
- [72] M. Yang, S. Li, Y. Wang, J.A. Herron, Y. Xu, L.F. Allard, S. Lee, J. Huang, M. Mavrikakis, M. Flytzani-Stephanopoulos, Catalytically active Au-O(OH)_x species stabilized by alkali ions on zeolites and mesoporous oxides, Science 346 (2014) 1498–1501, <https://doi.org/10.1126/science.1260526>.
- [73] E. Bayram, J. Lu, C. Aydin, N.D. Browning, S. Özkaz, E. Finney, B.C. Gates, R.G. Finke, Agglomerative sintering of an atomically dispersed Ir 1/zeolite Y catalyst: compelling evidence against ostwald ripening but for bimolecular and autocatalytic agglomeration catalyst sintering steps, ACS Catal. 5 (2015) 3514–3527, <https://doi.org/10.1021/acscatal.5b00321>.
- [74] Q. Sun, N. Wang, T. Zhang, R. Bai, A. Mayoral, P. Zhang, Q. Zhang, O. Terasaki, J. Yu, Zeolite-encaged single-atom rhodium catalysts: highly-efficient hydrogen generation and shape-selective tandem hydrogenation of nitroarenes, Angew. Chem. Int. Ed. 58 (2019) 18570–18576, <https://doi.org/10.1002/anie.201912367>.
- [75] Y. Liu, Z. Li, Q. Yu, Y. Chen, Z. Chai, G. Zhao, S. Liu, W.-C. Cheong, Y. Pan, Q. Zhang, L. Gu, L. Zheng, Y. Wang, Y. Lu, D. Wang, C. Chen, Q. Peng, Y. Liu, L. Liu, J. Chen, Y. Li, A general strategy for fabricating isolated single metal atomic site catalysts in Y zeolite, J. Am. Chem. Soc. 141 (2019) 9305–9311, <https://doi.org/10.1021/jacs.9b02936>.
- [76] L. Liu, N. Wang, C. Zhu, X. Liu, Y. Zhu, P. Guo, L. Alfilif, X. Dong, D. Zhang, Y. Han, Direct imaging of atomically dispersed molybdenum that enables location of aluminum in the framework of zeolite ZSM-5, Angew. Chem. Int. Ed. 59 (2020) 819–825, <https://doi.org/10.1002/anie.201909834>.
- [77] N.A. Grosso-Giordano, A.S. Hoffman, A. Boubnov, D.W. Small, S.R. Bare, S.I. Zones, A. Katz, Dynamic reorganization and confinement of Ti^{IV} active sites controls olefin epoxidation catalysis on two-dimensional zeotypes, J. Am. Chem. Soc. 141 (2019) 7090–7106, <https://doi.org/10.1021/jacs.9b02160>.
- [78] S. Wannakao, T. Maihom, M. Probst, J. Limtrakul, K. Kongpatpanich, Porous materials as a platform for highly uniform single-atom catalysts: tuning the electronic structure for the low-temperature oxidation of carbon monoxide, J. Phys. Chem. C 120 (2016) 19686–19697, <https://doi.org/10.1021/acs.jpcc.6b05205>.
- [79] H. Yan, H. Cheng, H. Yi, Y. Lin, T. Yao, C. Wang, J. Li, S. Wei, J. Lu, Single-atom Pd₁/graphene catalyst achieved by atomic layer deposition: remarkable performance in selective hydrogenation of 1,3-butadiene, J. Am. Chem. Soc. 137 (2015) 10484–10487, <https://doi.org/10.1021/jacs.5b06485>.
- [80] Y. Lou, Y. Zheng, X. Li, N. Ta, J. Xu, Y. Nie, K. Cho, J. Liu, Pocketlike active site of Rh₁/MoS₂ single-atom catalyst for selective crotonaldehyde hydrogenation, J. Am. Chem. Soc. 141 (2019) 19289–19295, <https://doi.org/10.1021/jacs.9b06628>.
- [81] J. Zhang, Y. Zhao, X. Guo, C. Chen, C.-L. Dong, R.-S. Liu, C.-P. Han, Y. Li, Y. Gogotsi, G. Wang, Single platinum atoms immobilized on an MXene as an efficient catalyst for the hydrogen evolution reaction, Nat. Catal. 1 (2018) 985–992, <https://doi.org/10.1038/s41929-018-0195-1>.

- [82] S. Ji, Y. Chen, X. Wang, Z. Zhang, D. Wang, Y. Li, Chemical synthesis of single atomic site catalysts, *Chem. Rev.* 120 (2020) 11900–11955, <https://doi.org/10.1021/ACS.CHEMREV.9B00818>.
- [83] R. Qin, K. Liu, Q. Wu, N. Zheng, Surface coordination chemistry of atomically dispersed metal catalysts, *Chem. Rev.* 120 (2020) 11810–11899, <https://doi.org/10.1021/ACS.CHEMREV.0C00094>.
- [84] Y.S. Wei, M. Zhang, R. Zou, Q. Xu, Metal-organic framework-based catalysts with single metal sites, *Chem. Rev.* 120 (2020) 12089–12174, <https://doi.org/10.1021/ACS.CHEMREV.9B00757>.
- [85] J. Li, M.F. Stephanopoulos, Y. Xia, Introduction: heterogeneous single-atom catalysis, *Chem. Rev.* 120 (2020) 11699–11702, <https://doi.org/10.1021/acs.chemrev.0c01097>.
- [86] M. Babucci, A. Guntida, B.C. Gates, Atomically dispersed metals on well-defined supports including zeolites and metal-organic frameworks: structure, bonding, reactivity, and catalysis, *Chem. Rev.* 120 (2020) 11956–11985, <https://doi.org/10.1021/ACS.CHEMREV.0C00864>.
- [87] L.F. Allard, A. Borisevich, W. Deng, R. Si, M. Flytzani-Stephanopoulos, S.H. Overbury, Evolution of gold structure during thermal treatment of Au/FeOx catalysts revealed by aberration-corrected electron microscopy, *J. Electron. Microsc. (Tokyo)* 58 (2009) 199–212, <https://doi.org/10.1093/jmicro/dfp016>.
- [88] Y. Zhao, K.R. Yang, Z. Wang, X. Yan, S. Cao, Y. Ye, Q. Dong, X. Zhang, J.E. Thorne, L. Jin, K.L. Materna, A. Trimpalis, H. Bai, S.C. Fakra, X. Zhong, P. Wang, X. Pan, J. Guo, M. Flytzani-Stephanopoulos, G.W. Brudvig, V.S. Batista, D. Wang, Stable iridium dinuclear heterogeneous catalysts supported on metal-oxide substrate for solar water oxidation, *Proc. Natl. Acad. Sci. U S A* 115 (2018) 2902–2907, <https://doi.org/10.1073/pnas.1722137115>.
- [89] J. Lin, B. Qiao, J. Liu, Y. Huang, A. Wang, L. Li, W. Zhang, L.F. Allard, X. Wang, T. Zhang, Design of a highly active Ir/Fe(OH)_x catalyst: versatile application of Pt-group metals for the preferential oxidation of carbon monoxide, *Angew. Chem. Int. Ed.* 51 (2012) 2920–2924, <https://doi.org/10.1002/anie.201106702>.
- [90] Y. Tang, C. Asokan, M. Xu, G.W. Graham, X. Pan, P. Christopher, J. Li, P. Sautet, Rh single atoms on TiO₂ dynamically respond to reaction conditions by adapting their site, *Nat. Commun.* 10 (2019) 4488, <https://doi.org/10.1038/s41467-019-12461-6>.
- [91] B.-H. Lee, S. Park, M. Kim, A.K. Sinha, S.C. Lee, E. Jung, W.J. Chang, K.-S. Lee, J.H. Kim, S.-P. Cho, H. Kim, K.T. Nam, T. Hyeon, Reversible and cooperative photoactivation of single-atom Cu/TiO₂ photocatalysts, *Nat. Mater.* 18 (2019) 620–626, <https://doi.org/10.1038/s41563-019-0344-1>.
- [92] B. Han, T. Li, J. Zhang, C. Zeng, H. Matsumoto, Y. Su, B. Qiao, T. Zhang, A highly active Rh₁/CeO₂ single-atom catalyst for low-temperature CO oxidation, *Chem. Commun.* 56 (2020) 4870–4873, <https://doi.org/10.1039/D0CC00230E>.
- [93] H. Jeong, G. Lee, B.-S. Kim, J. Bae, J.W. Han, H. Lee, Fully dispersed Rh ensemble catalyst to enhance low-temperature activity, *J. Am. Chem. Soc.* 140 (2018) 9558–9565, <https://doi.org/10.1021/jacs.8b04613>.
- [94] Z. Zhang, Q. Wu, G. Johnson, Y. Ye, X. Li, N. Li, M. Cui, J.D. Lee, C. Liu, S. Zhao, S. Li, A. Orlov, C.B. Murray, X. Zhang, T.B. Gunnoe, D. Su, S. Zhang, Generalized synthetic strategy for transition-metal-doped brookite-phase TiO₂ nanorods, *J. Am. Chem. Soc.* 141 (2019) 16548–16552, <https://doi.org/10.1021/jacs.9b06389>.
- [95] Y. Tang, Y. Wei, Z. Wang, S. Zhang, Y. Li, L. Nguyen, Y. Li, Y. Zhou, W. Shen, F.F. Tao, P. Hu, Synergy of single-atom Ni₁ and Ru₁ sites on CeO₂ for dry reforming of CH₄, *J. Am. Chem. Soc.* 141 (2019) 7283–7293, <https://doi.org/10.1021/jacs.8b10910>.
- [96] Q. Li, Z. Huang, P. Guan, R. Su, Q. Cao, Y. Chao, W. Shen, J. Guo, H. Xu, R. Che, Simultaneous Ni doping at atom scale in ceria and assembling into well-defined lotuslike structure for enhanced catalytic performance, *ACS Appl. Mater. Interfaces* 9 (2017) 16243–16251, <https://doi.org/10.1021/acsami.7b03394>.
- [97] L. Yuan, S.-F. Hung, Z.-R. Tang, H.M. Chen, Y. Xiong, Y.-J. Xu, Dynamic evolution of atomically dispersed Cu species for CO₂ photoreduction to solar fuels, *ACS Catal.* 9 (2019) 4824–4833, <https://doi.org/10.1021/acscatal.9b00862>.
- [98] Y. Wang, Z. Chen, P. Han, Y. Du, Z. Gu, X. Xu, G. Zheng, Single-atomic Cu with multiple oxygen vacancies on ceria for electrocatalytic CO₂ reduction to CH₄, *ACS Catal.* 8 (2018) 7113–7119, <https://doi.org/10.1021/acscatal.8b01014>.
- [99] W.-Z. Yu, W.-W. Wang, S.-Q. Li, X.-P. Fu, X. Wang, K. Wu, R. Si, C.-J. Jia, C.-H. Yan, Construction of active site in a sintered copper-ceria nanorod catalyst, *J. Am. Chem. Soc.* 141 (2019) 17548–17557, <https://doi.org/10.1021/jacs.9b05419>.
- [100] M.D. Marcinkowski, J. Liu, C.J. Murphy, M.L. Liriano, N.A. Wasio, F.R. Lucci, M. Flytzani-Stephanopoulos, E.C.H. Sykes, Selective formic acid dehydrogenation on Pt-Cu single-atom alloys, *ACS Catal.* 7 (2017) 413–420, <https://doi.org/10.1021/acscatal.6b02772>.
- [101] K. Otake, Y. Cui, C.T. Buru, Z. Li, J.T. Hupp, O.K. Farha, Single-atom-based vanadium oxide catalysts supported on metal-organic frameworks: selective alcohol oxidation and structure-activity relationship, *J. Am. Chem. Soc.* 140 (2018) 8652–8656, <https://doi.org/10.1021/jacs.8b05107>.
- [102] D. Deng, X. Chen, L. Yu, X. Wu, Q. Liu, Y. Liu, H. Yang, H. Tian, Y. Hu, P. Du, R. Si, J. Wang, X. Cui, H. Li, J. Xiao, T. Xu, J. Deng, F. Yang, P.N. Duchesne, P. Zhang, J. Zhou, L. Sun, J. Li, X. Pan, X. Bao, A single iron site confined in a graphene matrix for the catalytic oxidation of benzene at room temperature, *Sci. Adv.* 1 (2015), <https://doi.org/10.1126/sciadv.1500462>.
- [103] J. Xie, R. Jin, A. Li, Y. Bi, Q. Ruan, Y. Deng, Y. Zhang, S. Yao, G. Sankar, D. Ma, J. Tang, Highly selective oxidation of methane to methanol at ambient conditions by titanium dioxide-supported iron species, *Nat. Catal.* 1 (2018) 889–896, <https://doi.org/10.1038/s41929-018-0170-x>.
- [104] X. Sun, A.I. Olivos-Suarez, D. Osadchii, M.J.V. Romero, F. Kapteijn, J. Gascon, Single cobalt sites in mesoporous N-doped carbon matrix for selective catalytic hydrogenation of nitroarenes, *J. Catal.* 357 (2018) 20–28, <https://doi.org/10.1016/j.jcat.2017.10.030>.
- [105] M. Li, S. Wu, X. Yang, J. Hu, L. Peng, L. Bai, Q. Huo, J. Guan, Highly efficient single atom cobalt catalyst for selective oxidation of alcohols, *Appl. Catal. A Gen.* 543 (2017) 61–66, <https://doi.org/10.1016/j.apcata.2017.06.018>.
- [106] K. Qi, X. Cui, L. Gu, S. Yu, X. Fan, M. Luo, S. Xu, N. Li, L. Zheng, Q. Zhang, J. Ma, Y. Gong, F. Lv, K. Wang, H. Huang, W. Zhang, S. Guo, W. Zheng, P. Liu, Single-atom cobalt array bound to distorted 1T MoS₂ with ensemble effect for hydrogen evolution catalysis, *Nat. Commun.* 10 (2019) 5231, <https://doi.org/10.1038/s41467-019-12997-7>.
- [107] J. Di, C. Chen, S.-Z. Yang, S. Chen, M. Duan, J. Xiong, C. Zhu, R. Long, W. Hao, Z. Chi, H. Chen, Y.-X. Weng, J. Xia, L. Song, S. Li, H. Li, Z. Liu, Isolated single atom cobalt in Bi₂O₃/Br atomic layers to trigger efficient CO₂ photoreduction, *Nat. Commun.* 10 (2019) 2840, <https://doi.org/10.1038/s41467-019-10392-w>.
- [108] M. Yang, H. Qi, F. Liu, Y. Ren, X. Pan, L. Zhang, X. Liu, H. Wang, J. Pang, M. Zheng, A. Wang, T. Zhang, One-pot production of cellulosic ethanol via tandem catalysis over a multifunctional Mo/Pt/WO_x catalyst, *Joule* 3 (2019) 1937–1948, <https://doi.org/10.1016/j.joule.2019.05.020>.
- [109] C. Aydin, A. Kulkarni, M. Chi, N.D. Browning, B.C. Gates, Atomically resolved site-isolated catalyst on MgO: mononuclear osmium dicarbonyls formed from Os₃(CO)₁₂, *J. Phys. Chem. Lett.* 3 (2012) 1865–1871, <https://doi.org/10.1021/jz300574u>.
- [110] V. Vidal, A. Théolier, J. Thivolle-Cazat, J.-M. Basset, Metathesis of alkanes catalyzed by silica-supported transition metal hydrides, *Science* 276 (1997) 99–102, <https://doi.org/10.1126/science.276.5309.99>.
- [111] P. Zhao, L. Ye, Z. Sun, B.T.W. Lo, H. Woodcock, C. Huang, C. Tang, A.I. Kirkland, D. Mei, S.C. Edman Tsang, Entrapped single tungstate site in zeolite for cooperative catalysis of olefin metathesis with Brønsted acid site, *J. Am. Chem. Soc.* 140 (2018) 6661–6667, <https://doi.org/10.1021/jacs.8b03012>.
- [112] S. Wang, A.Y. Borisevich, S.N. Rashkeev, M.V. Glazoff, K. Söhlberg, S.J. Pennycook, S.T. Pantelides, Dopants adsorbed as single atoms prevent degradation of catalysts, *Nat. Mater.* 3 (3) (2004) 143–146, <https://doi.org/10.1038/nmat1077>.
- [113] H.N. Pham, J.J.H.B. Sattler, B.M. Weckhuysen, A.K. Datye, Role of Sn in the regeneration of Pt/γ-Al₂O₃ light alkane dehydrogenation catalysts, *ACS Catal.* 6 (2016) 2257–2264, <https://doi.org/10.1021/acscatal.5b02917>.
- [114] Y. Zhu, Z. An, J. He, Single-atom and small-cluster Pt induced by Sn (IV) sites confined in an LDH lattice for catalytic reforming, *J. Catal.* 341 (2016) 44–54, <https://doi.org/10.1016/j.jcat.2016.06.004>.
- [115] L. Rochlitz, K. Searles, J. Alfke, D. Zemlyanov, O.V. Safonova, C. Copéret, Silica-supported, narrowly distributed, subnanometric Pt–Zn particles from single sites with high propane dehydrogenation performance, *Chem. Sci.* 11 (6) (2020) 1549–1555, <https://doi.org/10.1039/C9SC05599A>.
- [116] C. Riley, S. Zhou, D. Kunwar, A. de La Riva, E. Peterson, R. Payne, L. Gao, S. Lin, H. Guo, A. Datye, Design of effective catalysts for selective alkyne hydrogenation by doping of ceria with a single-atom promoter, *J. Am. Chem. Soc.* 140 (2018) 12964–12973, <https://doi.org/10.1021/JACS.8B07789>.
- [117] Y.F. Li, W. Lu, K. Chen, P. Duchesne, A. Jelle, M. Xia, T.E. Wood, U. Ulmer, G.A. Ozin, Cu atoms on nanowire Pd/H₂WO_{3-x} bronzes enhance the solar reverse water gas shift reaction, *J. Am. Chem. Soc.* 141 (2019) 14991–14996, <https://doi.org/10.1021/jacs.9b08030>.
- [118] E. Lam, K. Larmier, P. Wolf, S. Tada, O.V. Safonova, C. Copéret, Isolated Zr surface sites on silica promote hydrogenation of CO₂ to CH₃OH in supported Cu catalysts, *J. Am. Chem. Soc.* 140 (33) (2018) 10530–10535, <https://doi.org/10.1021/jacs.8b05595>.
- [119] L. Cao, W. Liu, Q. Luo, R. Yin, B. Wang, J. Weissenrieder, M. Soldemo, H. Yan, Y. Lin, Z. Sun, C. Ma, W. Zhang, S. Chen, H. Wang, Q. Guan, T. Yao, S. Wei, J. Yang, J. Lu, Atomically dispersed iron hydroxide anchored on Pt for preferential oxidation of CO in H₂, *Nature* 565 (2019) 631–635, <https://doi.org/10.1038/s41586-018-0869-5>.
- [120] M.B. Boucher, B. Zucig, G. Cladaras, J. Kammert, M.D. Marcinkowski, T.J. Lawton, E.C.H. Sykes, M. Flytzani-Stephanopoulos, Single atom alloy surface analogs in Pd_{0.18}Cu_{0.15} nanoparticles for selective hydrogenation reactions, *Phys. Chem. Chem. Phys.* 15 (2013) 12187, <https://doi.org/10.1039/c3cp51538a>.
- [121] M.T. Darby, M. Stamatakis, A. Michaelides, E. Charles, H. Sykes, Lonely atoms with special gifts: breaking linear scaling relationships in heterogeneous catalysis with single-atom alloys, *J. Phys. Chem. Lett.* 9 (2018) 5636–5646, <https://doi.org/10.1021/acs.jpcclett.8b01888>.
- [122] G. Giannakakis, M. Flytzani-Stephanopoulos, E.C.H. Sykes, Single-atom alloys as a reductionist approach to the rational design of heterogeneous catalysts, *Acc. Chem. Res.* 52 (2019) 237–247, <https://doi.org/10.1021/acs.accounts.8b00490>.
- [123] W. Xu, R. Si, S.D. Senanayake, J. Llorca, H. Idriss, D. Stacchiola, J.C. Hanson, J.A. Rodriguez, In situ studies of CeO₂-supported Pt, Ru, and Pt–Ru alloy catalysts for the water–gas shift reaction: active phases and reaction intermediates, *J. Catal.* 291 (2012) 117–126, <https://doi.org/10.1016/j.jcat.2012.04.013>.
- [124] T. Magadzu, J.H. Yang, J.D. Heno, M.C. Kung, H.H. Kung, M.S. Scurrell, Low-temperature water–gas shift reaction over Au supported on anatase in the presence of copper: EXAFS/XANES analysis of gold–copper ion mixtures on TiO₂, *J. Phys. Chem. C* 121 (2017) 8812–8823, <https://doi.org/10.1021/acs.jpcc.6b11419>.

- [125] S.C. Ammal, A. Heyden, Water-gas shift activity of atomically dispersed cationic platinum versus metallic platinum clusters on titania supports, *ACS Catal.* 7 (2017) 301–309, <https://doi.org/10.1021/acscatal.6b02764>.
- [126] W. Huang, S. Zhang, Y. Tang, Y. Li, L. Nguyen, Y. Li, J. Shan, D. Xiao, R. Gagne, A. I. Frenkel, F.F. Tao, Low-temperature transformation of methane to methanol on Pd₂O₄ single sites anchored on the internal surface of microporous silicate, *Angew. Chem. Int. Ed.* 55 (2016) 13441–13445, <https://doi.org/10.1002/anie.201604708>.
- [127] J. Shan, M. Li, L.F. Allard, S. Lee, M. Flytzani-Stephanopoulos, Mild oxidation of methane to methanol or acetic acid on supported isolated rhodium catalysts, *Nature* 551 (2017) 605–608, <https://doi.org/10.1038/nature24640>.
- [128] J. Shan, F.R. Lucci, J. Liu, M. El-Soda, M.D. Marcinkowski, L.F. Allard, E.C.H. Sykes, M. Flytzani-Stephanopoulos, Water co-catalyzed selective dehydrogenation of methanol to formaldehyde and hydrogen, *Surf. Sci.* 650 (2016) 121–129, <https://doi.org/10.1016/j.susc.2016.02.010>.
- [129] G. Kyriakou, M.B. Boucher, A.D. Jewell, E.A. Lewis, T.J. Lawton, A.E. Baber, H.L. Tierney, M. Flytzani-Stephanopoulos, E.C.H. Sykes, Isolated metal atom geometries as a strategy for selective heterogeneous hydrogenations, *Science* 335 (2012) (1979) 1209–1212, <https://doi.org/10.1126/science.1215864>.
- [130] G.X. Pei, X.Y. Liu, X. Yang, L. Zhang, A. Wang, L. Li, H. Wang, X. Wang, T. Zhang, Performance of Cu-alloyed Pd single-atom catalyst for semihydrogenation of acetylene under simulated front-end conditions, *ACS Catal.* 7 (2017) 1491–1500, <https://doi.org/10.1021/acscatal.6b03293>.
- [131] X. Zhang, Z. Sun, B. Wang, Y. Tang, L. Nguyen, Y. Li, F.F. Tao, C-C Coupling on single-atom-based heterogeneous catalyst, *J. Am. Chem. Soc.* 140 (2018) 954–962, <https://doi.org/10.1021/jacs.7b09314>.
- [132] P. Xie, T. Pu, A. Nie, S. Hwang, S.C. Purdy, W. Yu, D. Su, J.T. Miller, C. Wang, Nanoceria-supported single-atom platinum catalysts for direct methane conversion, *ACS Catal.* 8 (2018) 4044–4048, <https://doi.org/10.1021/acscatal.8b00004>.
- [133] X. Guo, G. Fang, G. Li, H. Ma, H. Fan, L. Yu, C. Ma, X. Wu, D. Deng, M. Wei, D. Tan, R. Si, S. Zhang, J. Li, L. Sun, Z. Tang, X. Pan, X. Bao, Direct, nonoxidative conversion of methane to ethylene, aromatics, and hydrogen, *Science* 344 (2014) (1979) 616–619, <https://doi.org/10.1126/science.1253150>.
- [134] Y. Chen, S. Ji, W. Sun, W. Chen, J. Dong, J. Wen, J. Zhang, Z. Li, L. Zheng, C. Chen, Q. Peng, D. Wang, Y. Li, Discovering partially charged single-atom Pt for enhanced anti-markovnikov alkene hydrosilylation, *J. Am. Chem. Soc.* 140 (2018) 7407–7410, <https://doi.org/10.1021/jacs.8b03121>.
- [135] H. Miura, K. Endo, R. Ogawa, T. Shishido, Supported palladium-gold alloy catalysts for efficient and selective hydrosilylation under mild conditions with isolated single palladium atoms in alloy nanoparticles as the main active site, *ACS Catal.* 7 (2017) 1543–1553, <https://doi.org/10.1021/acscatal.6b02767>.
- [136] X. Cui, K. Junge, X. Dai, C. Kreyenschulte, M.-M. Pohl, S. Wohlrab, F. Shi, A. Brückner, M. Beller, Synthesis of single atom based heterogeneous platinum catalysts: high selectivity and activity for hydrosilylation reactions, *ACS Cent. Sci.* 3 (2017) 580–585, <https://doi.org/10.1021/acscentsci.7b00105>.
- [137] W. Lai, L. Zhang, W. Hua, S. Indris, Z. Yan, Z. Hu, B. Zhang, Y. Liu, L. Wang, M. Liu, R. Liu, Y. Wang, J. Wang, Z. Hu, H. Liu, S. Chou, S. Dou, General π -electron-assisted strategy for Ir, Pt, Ru, Pd, Fe, Ni single-atom electrocatalysts with bifunctional active sites for highly efficient water splitting, *Angew. Chem.* 131 (2019) 11994–11999, <https://doi.org/10.1002/ange.201904614>.
- [138] B. Lu, L. Guo, F. Wu, Y. Peng, J.E. Lu, T.J. Smart, N. Wang, Y.Z. Finrock, D. Morris, P. Zhang, N. Li, P. Gao, Y. Ping, S. Chen, Ruthenium atomically dispersed in carbon outperforms platinum toward hydrogen evolution in alkaline media, *Nat. Commun.* 10 (2019) 631, <https://doi.org/10.1038/s41467-019-08419-3>.
- [139] J. Deng, H. Li, J. Xiao, Y. Tu, D. Deng, H. Yang, H. Tian, J. Li, P. Ren, X. Bao, Triggering the electrocatalytic hydrogen evolution activity of the inert two-dimensional MoS₂ surface via single-atom metal doping, *Energy Environ. Sci.* 8 (2015) 1594–1601, <https://doi.org/10.1039/C5EE00751H>.
- [140] J. Zhang, J. Liu, L. Xi, Y. Yu, N. Chen, S. Sun, W. Wang, K.M. Lange, B. Zhang, Single-atom Au/NiFe layered double hydroxide electrocatalyst: probing the origin of activity for oxygen evolution reaction, *J. Am. Chem. Soc.* 140 (2018) 3876–3879, <https://doi.org/10.1021/jacs.8b00752>.
- [141] H. Fei, J. Dong, Y. Feng, C.S. Allen, C. Wan, B. Voloskiy, M. Li, Z. Zhao, Y. Wang, H. Sun, P. An, W. Chen, Z. Guo, C. Lee, D. Chen, I. Shakir, M. Liu, T. Hu, Y. Li, A.I. Kirkland, X. Duan, Y. Huang, General synthesis and definitive structural identification of MN₄C₄ single-atom catalysts with tunable electrocatalytic activities, *Nat. Catal.* 1 (2018) 63–72, <https://doi.org/10.1038/s41929-017-0008-y>.
- [142] P. Li, M. Wang, X. Duan, L. Zheng, X. Cheng, Y. Zhang, Y. Kuang, Y. Li, Q. Ma, Z. Feng, W. Liu, X. Sun, Boosting oxygen evolution of single-atomic ruthenium through electronic coupling with cobalt-iron layered double hydroxides, *Nat. Commun.* 10 (2019) 1711, <https://doi.org/10.1038/s41467-019-09666-0>.
- [143] F. He, K. Li, C. Yin, Y. Wang, H. Tang, Z. Wu, Single Pd atoms supported by graphitic carbon nitride, a potential oxygen reduction reaction catalyst from theoretical perspective, *Carbon* 114 (2017) 619–627, <https://doi.org/10.1016/j.carbon.2016.12.061>.
- [144] M. Xiao, J. Zhu, G. Li, N. Li, S. Li, Z.P. Cano, L. Ma, P. Cui, P. Xu, G. Jiang, H. Jin, S. Wang, T. Wu, J. Lu, A. Yu, D. Su, Z. Chen, A single-atom iridium heterogeneous catalyst in oxygen reduction reaction, *Angew. Chem.* 131 (2019) 9742–9747, <https://doi.org/10.1002/ange.201905241>.
- [145] J. Liu, M. Jiao, L. Lu, H.M. Barkholtz, Y. Li, Y. Wang, L. Jiang, Z. Wu, D. Liu, L. Zhuang, C. Ma, J. Zeng, B. Zhang, D. Su, P. Song, W. Xing, W. Xu, Y. Wang, Z. Jiang, G. Sun, High performance platinum single atom electrocatalyst for oxygen reduction reaction, *Nat. Commun.* 8 (2017) 15938, <https://doi.org/10.1038/ncomms15938>.
- [146] W. Zheng, J. Yang, H. Chen, Y. Hou, Q. Wang, M. Gu, F. He, Y. Xia, Z. Xia, Z. Li, B. Yang, L. Lei, C. Yuan, Q. He, M. Qiu, X. Feng, Atomically defined undercoordinated active sites for highly efficient CO₂ electroreduction, *Adv. Funct. Mater.* 30 (2020) 1907658, <https://doi.org/10.1002/adfm.201907658>.
- [147] X. Wang, Z. Chen, X. Zhao, T. Yao, W. Chen, R. You, C. Zhao, G. Wu, J. Wang, W. Huang, J. Yang, X. Hong, S. Wei, Y. Wu, Y. Li, Regulation of Coordination Number over Single Co Sites: Triggering the Efficient Electroreduction of CO₂, *Angewandte Chemie International Edition.* 57 (2018) 1944–1948, <https://doi.org/10.1002/anie.201712451>.
- [148] S. Liu, H.B. Yang, S.-F. Hung, J. Ding, W. Cai, L. Liu, J. Gao, X. Li, X. Ren, Z. Kuang, Y. Huang, T. Zhang, B. Liu, Elucidating the electrocatalytic CO₂ reduction reaction over a model single-atom nickel catalyst, *Angew. Chem.* 132 (2) (2020) 808–813, <https://doi.org/10.1002/ange.201911995>.
- [149] J. Zhao, J. Zhao, Q. Cai, Single transition metal atom embedded into a MoS₂ nanosheet as a promising catalyst for electrochemical ammonia synthesis, *Phys. Chem. Chem. Phys.* 20 (2018) 9248–9255, <https://doi.org/10.1039/C7CP08626A>.
- [150] Q. Qin, T. Heil, M. Antonietti, M. Oschatz, Single-site gold catalysts on hierarchical N-doped porous noble carbon for enhanced electrochemical reduction of nitrogen, *Small Methods* 2 (2018) 1800202, <https://doi.org/10.1002/smt.201800202>.
- [151] Z. Geng, Y. Liu, X. Kong, P. Li, K. Li, Z. Liu, J. Du, M. Shu, R. Si, J. Zeng, Achieving a record-high yield rate of 120.9 $\mu\text{g}_{\text{NH}_3} \text{mg}_{\text{cat}}^{-1} \text{h}^{-1}$ for N₂ electrochemical reduction over Ru single-atom catalysts, *Adv. Mater.* 30 (2018) 1803498, <https://doi.org/10.1002/adma.201803498>.
- [152] S. Cao, H. Li, T. Tong, H.-C. Chen, A. Yu, J. Yu, H.M. Chen, Single-atom engineering of directional charge transfer channels and active sites for photocatalytic hydrogen evolution, *Adv. Funct. Mater.* 28 (2018) 1802169, <https://doi.org/10.1002/adfm.201802169>.
- [153] X. Wu, H. Zhang, J. Dong, M. Qiu, J. Kong, Y. Zhang, Y. Li, G. Xu, J. Zhang, J. Ye, Surface step decoration of isolated atom as electron pumping: atomic-level insights into visible-light hydrogen evolution, *Nano Energy* 45 (2018) 109–117, <https://doi.org/10.1016/j.nanoen.2017.12.039>.
- [154] X. Li, W. Bi, L. Zhang, S. Tao, W. Chu, Q. Zhang, Y. Luo, C. Wu, Y. Xie, Single-atom Pt as Co-catalyst for enhanced photocatalytic H₂ evolution, *Adv. Mater.* 28 (2016) 2427–2431, <https://doi.org/10.1002/adma.201505281>.
- [155] P. Huang, J. Huang, S.A. Pantovich, A.D. Carl, T.G. Fenton, C.A. Caputo, R.L. Grimm, A.I. Frenkel, G. Li, Selective CO₂ reduction catalyzed by single cobalt sites on carbon nitride under visible-light irradiation, *J. Am. Chem. Soc.* 140 (2018) 16042–16047, <https://doi.org/10.1021/jacs.8b10380>.
- [156] X. Li, W. Bi, Z. Wang, W. Zhu, W. Chu, C. Wu, Y. Xie, Surface-adsorbed ions on TiO₂ nanosheets for selective photocatalytic CO₂ reduction, *Nano Res.* 11 (2018) 3362–3370, <https://doi.org/10.1007/s12274-017-1933-4>.
- [157] S. Liu, Y. Wang, S. Wang, M. You, S. Hong, T.-S. Wu, Y.-L. Soo, Z. Zhao, G. Jiang, Jieshan Qiu, B. Wang, Z. Sun, Photocatalytic fixation of nitrogen to ammonia by single Ru atom decorated TiO₂ nanosheets, *ACS Sustain. Chem. Eng.* 7 (7) (2019) 6813–6820, <https://doi.org/10.1021/acssuschemeng.8b06134>.
- [158] X.-W. Guo, S.-M. Chen, H.-J. Wang, Z.-M. Zhang, H. Lin, L. Song, T.-B. Lu, Single-atom molybdenum immobilized on photoactive carbon nitride as efficient photocatalysts for ambient nitrogen fixation in pure water, *J. Mater. Chem. A Mater.* 7 (2019) 19831–19837, <https://doi.org/10.1039/C9TA06653E>.
- [159] W. Wu, E. Cui, Y. Zhang, C. Zhang, F. Zhu, C.-H. Tung, Y. Wang, Involving single-atom silver(0) in selective dehalogenation by AgF under visible-light irradiation, *ACS Catal.* 9 (2019) 6335–6341, <https://doi.org/10.1021/acscatal.9b01929>.
- [160] S. An, G. Zhang, T. Wang, W. Zhang, K. Li, C. Song, J.T. Miller, S. Miao, J. Wang, X. Guo, High-density ultra-small clusters and single-atom Fe sites embedded in graphitic carbon nitride (g-C₃N₄) for highly efficient catalytic advanced oxidation processes, *ACS Nano.* 12 (2018) 9441–9450, <https://doi.org/10.1021/acsnano.8b04693>.
- [161] L. Collado, I. Jansson, A.E. Platero-Prats, V. Perez-Dieste, C. Escudero, E. Molins, L. Casas i Doucastela, B. Sánchez, J.M. Coronado, D.P. Serrano, S. Suarez, V.A. de la Peña-O'Shea, Elucidating the photoredox nature of isolated iron active sites on MCM-41, *ACS Catal.* 7 (3) (2017) 1646–1654, <https://doi.org/10.1021/acscatal.6b03208>.
- [162] F. Wang, Y. Wang, Y. Feng, Y. Zeng, Z. Xie, Q. Zhang, Y. Su, P. Chen, Y. Liu, K. Yao, W. Lv, G. Liu, Novel ternary photocatalyst of single atom-dispersed silver and carbon quantum dots co-loaded with ultrathin g-C₃N₄ for broad spectrum photocatalytic degradation of naproxen, *Appl. Catal. B* 221 (2018) 510–520, <https://doi.org/10.1016/j.apcatb.2017.09.055>.
- [163] X. Feng, Y. Song, J.S. Chen, Z. Li, E.Y. Chen, M. Kaufmann, C. Wang, W. Lin, Cobalt-bridged secondary building units in a titanium metal-organic framework catalyze cascade reduction of N-heteroarenes, *Chem. Sci.* 10 (2019) 2193–2198, <https://doi.org/10.1039/C8SC04610G>.
- [164] G. Wächtershäuser, Groundworks for an evolutionary biochemistry: the iron-sulphur world, *Prog. Biophys. Mol. Biol.* 58 (1992) 85–201, [https://doi.org/10.1016/0079-6107\(92\)90022-X](https://doi.org/10.1016/0079-6107(92)90022-X).
- [165] M.J. Russell, A.J. Hall, The emergence of life from iron monosulphide bubbles at a submarine hydrothermal redox and pH front, *J. Geol. Soc. London* 154 (1997) 377–402, <https://doi.org/10.1144/gsjgs.154.3.0377>.
- [166] A. Roldan, N. Hollingsworth, A. Roffey, H.-U. Islam, J.B.M. Goodall, C.R.A. Catlow, J.A. Darr, W. Bras, G. Sankar, K.B. Holt, G. Hogarth, N.H. de Leeuw, Bio-

- inspired CO₂ conversion by iron sulfide catalysts under sustainable conditions, *Chem. Commun.* 51 (2015) 7501–7504, <https://doi.org/10.1039/C5CC02078F>.
- [167] D. Santos-Carballal, A. Roldan, N.H. de Leeuw, CO₂ reduction to acetic acid on the greigite Fe₃S₄{111} surface, *Faraday Discuss.* 229 (2021) 35–49, <https://doi.org/10.1039/C9FD00141G>.
- [168] A. Roldan, N.H. de Leeuw, Selective hydrogenation of CO on Fe₃S₄{111}: a computational study, *Faraday Discuss.* 197 (2017) 325–336, <https://doi.org/10.1039/C6FD00224B>.
- [169] A. Roldan, N.H. de Leeuw, Catalytic water dissociation by greigite Fe₃S₄ surfaces: density functional theory study, *Proc. R. Soc. A.* 472 (2188) (2016) 20160080, <https://doi.org/10.1098/rspa.2016.0080>.
- [170] A. Roldan, N.H. de Leeuw, A density functional theory study of the hydrogenation and reduction of the thio-spinel Fe₃S₄{111} surface, *Phys. Chem. Chem. Phys.* 21 (2019) 2426–2433, <https://doi.org/10.1039/C8CP06371K>.
- [171] D. Santos-Carballal, A. Roldan, N.H. de Leeuw, Early oxidation processes on the greigite Fe₃S₄{001} surface by water: a density functional theory study, *J. Phys. Chem. C* 120 (2016) 8616–8629, <https://doi.org/10.1021/acs.jpcc.6b00216>.
- [172] S.N.A. Zakaria, N. Hollingsworth, H.U. Islam, A. Roffey, D. Santos-Carballal, A. Roldan, W. Bras, G. Sankar, G. Hogarth, K.B. Holt, N.H. de Leeuw, Insight into the nature of iron sulfide surfaces during the electrochemical hydrogen evolution and CO₂ reduction reactions, *ACS Appl. Mater. Interfaces* 10 (2018) 32078–32085, <https://doi.org/10.1021/acsami.8b08612>.
- [173] C.E. Mitchell, D. Santos-Carballal, A.M. Beale, W. Jones, D.J. Morgan, M. Sankar, N.H. de Leeuw, The role of surface oxidation and Fe–Ni synergy in Fe–Ni–S catalysts for CO₂ hydrogenation, *Faraday Discuss.* 230 (2021) 30–51, <https://doi.org/10.1039/D0FD00137F>.
- [174] D. Santos-Carballal, N.H. de Leeuw, Catalytic formation of oxalic acid on the partially oxidised greigite Fe₃S₄{001} surface, *Phys. Chem. Chem. Phys.* 24 (2022) 20104–20124, <https://doi.org/10.1039/D2CP00333C>.
- [175] W. He, Z. Li, J. Yang, J.G. Hou, Electronic structures of organic molecule encapsulated BN nanotubes under transverse electric field, *J. Chem. Phys.* 129 (2) (2008) 024710, <https://doi.org/10.1063/1.2946708>.
- [176] G. Pacchioni, J.R. Lomas, F. Illas, Electric field effects in heterogeneous catalysis, *J. Mol. Catal. A Chem.* 119 (1997) 263–273, [https://doi.org/10.1016/S1381-1169\(96\)00490-6](https://doi.org/10.1016/S1381-1169(96)00490-6).
- [177] F. Che, J.T. Gray, S. Ha, N. Kruse, S.L. Scott, J.-S. McEwen, Elucidating the roles of electric fields in catalysis: a perspective, *ACS Catal.* 8 (2018) 5153–5174, <https://doi.org/10.1021/acscatal.7b02899>.
- [178] M. Aresta, Chapter 1. Carbon Dioxide: Utilization Options to Reduce its Accumulation in the Atmosphere, in: M. Aresta (Ed.), *Carbon Dioxide as Chemical Feedstock*, Wiley-VCH Verlag GmbH & Co. KGaA, Weinheim, Germany, 2010, pp. 1–13, 10.1002/9783527629916.ch1.
- [179] G. Kresse, J. Hafner, Ab initio molecular dynamics for liquid metals, *Phys. Rev. B* 47 (1993) 558–561, <https://doi.org/10.1103/PhysRevB.47.558>.
- [180] G. Kresse, J. Hafner, Ab initio molecular-dynamics simulation of the liquid-metal–amorphous-semiconductor transition in germanium, *Phys. Rev. B* 49 (1994) 14251–14269, <https://doi.org/10.1103/PhysRevB.49.14251>.
- [181] G. Kresse, J. Furthmüller, Efficient iterative schemes for ab initio total-energy calculations using a plane-wave basis set, *Phys. Rev. B* 54 (1996) 11169–11186, <https://doi.org/10.1103/PhysRevB.54.11169>.
- [182] G. Kresse, J. Furthmüller, Efficiency of ab-initio total energy calculations for metals and semiconductors using a plane-wave basis set, *Comput. Mater. Sci.* 6 (1996) 15–50, [https://doi.org/10.1016/0927-0256\(96\)00008-0](https://doi.org/10.1016/0927-0256(96)00008-0).
- [183] J. Sun, A. Ruzsinszky, J. Perdew, Strongly constrained and appropriately normed semilocal density functional, *Phys. Rev. Lett.* 115 (2015) 1–6, <https://doi.org/10.1103/PhysRevLett.115.036402>.
- [184] P.E. Blöchl, Projector augmented-wave method, *Phys. Rev. B* 50 (1994) 17953–17979, <https://doi.org/10.1103/PhysRevB.50.17953>.
- [185] G. Kresse, D. Joubert, From ultrasoft pseudopotentials to the projector augmented-wave method, *Phys. Rev. B* 59 (1999) 1758–1775, <https://doi.org/10.1103/PhysRevB.59.1758>.
- [186] G.P. Kerker, Efficient iteration scheme for self-consistent pseudopotential calculations, *Phys. Rev. B* 23 (1981) 3082–3084, <https://doi.org/10.1103/PhysRevB.23.3082>.
- [187] P. Pulay, Convergence acceleration of iterative sequences. The case of SCF iteration, *Chem. Phys. Lett.* 73 (1980) 393–398, [https://doi.org/10.1016/0009-2614\(80\)80396-4](https://doi.org/10.1016/0009-2614(80)80396-4).
- [188] E.R. Davidson, Matrix eigenvector methods, in: G.H.F. Diercksen, S. Wilson (Eds.), *Methods in Computational Molecular Physics*, Springer, Netherlands, Dordrecht, 1983, pp. 95–113, https://doi.org/10.1007/978-94-009-7200-1_4.
- [189] E.R. Davidson, The iterative calculation of a few of the lowest eigenvalues and corresponding eigenvectors of large real-symmetric matrices, *J. Comput. Phys.* 17 (1975) 87–94, [https://doi.org/10.1016/0021-9991\(75\)90065-0](https://doi.org/10.1016/0021-9991(75)90065-0).
- [190] B. Liu, The simultaneous expansion-method for the iterative solution of several of the lowest eigenvalues and corresponding eigenvectors of large real-symmetric matrices, in: C. Moler, I. Shavitt (Eds.), *Report on the Workshop Numerical Algorithms in Chemistry: Algebraic Methods*, National Resource for Computation in Chemistry, Lawrence Berkeley Laboratory, University of California, Berkeley, 1978, pp. 49–53, <https://www.osti.gov/biblio/6169634> (accessed August 22, 2022).
- [191] S. Grimme, Semiempirical GGA-type density functional constructed with a long-range dispersion correction, *J. Comput. Chem.* 27 (2006) 1787–1799, <https://doi.org/10.1002/jcc.20495>.
- [192] D. Santos-Carballal, A. Cadi-Essadek, N.H. de Leeuw, Catalytic conversion of CO and H₂ into hydrocarbons on the cobalt Co(111) surface: implications for the Fischer-Tropsch process, *J. Phys. Chem. C* 125 (2021) 11891–11903, <https://doi.org/10.1021/acs.jpcc.1c00254>.
- [193] A. Cadi-Essadek, A. Roldan, D. Santos-Carballal, P.E. Ngoepe, M. Claeys, N.H. de Leeuw, DFT + U study of the electronic, magnetic and mechanical properties of Co, CoO, and Co₃O₄, *S. Afr. J. Chem.* 74 (2021) 8–16, <https://doi.org/10.17159/0379-4350/2021/v74a3>.
- [194] L.M. Botha, D. Santos-Carballal, U. Terranova, M.G. Quesne, M.J. Ungerer, C.G. C.E. van Sittert, N.H. de Leeuw, Mixing thermodynamics and electronic structure of the Pt_{1-x}Ni_x (0 ≤ x ≤ 1) bimetallic alloy, *RSC Adv.* 9 (2019) 16948–16954, <https://doi.org/10.1039/C9RA02320H>.
- [195] B. Ramogayana, D. Santos-Carballal, P.A. Aparicio, M.G. Quesne, K.P. Maeneta, P.E. Ngoepe, N.H. de Leeuw, Ethylene carbonate adsorption on the major surfaces of lithium manganese oxide Li_{1-x}Mn₂O₄ spinel (0.000 < x < 0.375): a DFT + U – D3 study, *Phys. Chem. Chem. Phys.* 22 (2020) 6763–6771, <https://doi.org/10.1039/C9CP05658K>.
- [196] A. Vahl, O. Lupan, D. Santos-Carballal, V. Postica, S. Hansen, H. Cavers, N. Wolff, M.-I. Terasa, M. Hoppe, A. Cadi-Essadek, T. Dankwort, L. Kienle, N.H. de Leeuw, R. Adelung, F. Faupel, Surface functionalization of ZnO: Ag columnar thin films with AgAu and AgPt bimetallic alloy nanoparticles as an efficient pathway for highly sensitive gas discrimination and early hazard detection in batteries, *J. Mater. Chem. A Mater.* 8 (2020) 16246–16264, <https://doi.org/10.1039/D0TA03224G>.
- [197] L. Reguera, N.L. López, J. Rodríguez-Hernández, M. González, C.E. Hernandez-Tamargo, D. Santos-Carballal, N.H. de Leeuw, E. Reguera, Synthesis, crystal structures, and properties of zeolite-Like T₃(H₂O)₂M(CN)₆·uH₂O (T = Co, Zn; M = Ru, Os), *Eur. J. Inorg. Chem.* 2017 (2017) 2980–2989, <https://doi.org/10.1002/ejic.201700278>.
- [198] K.T. Malatji, D. Santos-Carballal, U. Terranova, P.E. Ngoepe, N.H. de Leeuw, Controlling the lithium intercalation voltage in the Li(Mn_{1-x}Ni_x)₂O₄ spinel via tuning of the Ni concentration: a density functional theory study, *S. Afr. J. Chem.* 74 (2021) 3–7, <https://doi.org/10.17159/0379-4350/2021/v74a2>.
- [199] D. Santos-Carballal, P.E. Ngoepe, N.H. de Leeuw, Ab initio investigation of the thermodynamics of cation distribution and of the electronic and magnetic structures in the LiMn₂O₄ spinel, *Phys. Rev. B* 97 (2018), <https://doi.org/10.1103/PhysRevB.97.085126>.
- [200] S. Posada-Pérez, D. Santos-Carballal, U. Terranova, A. Roldan, F. Illas, N.H. de Leeuw, CO₂ Interaction with violarite (FeNi₂S₄) surfaces: a dispersion-corrected DFT study, *Phys. Chem. Chem. Phys.* 20 (2018) 20439–20446, <https://doi.org/10.1039/C8CP03430C>.
- [201] Y. Zhang, J. Sun, J.P. Perdew, X. Wu, Comparative first-principles studies of prototypical ferroelectric materials by LDA, GGA, and SCAN meta-GGA, *Phys. Rev. B* 96 (2017), <https://doi.org/10.1103/PhysRevB.96.035143>.
- [202] G. Sai Gautam, E.A. Carter, Evaluating transition metal oxides within DFT-SCAN and SCAN + U frameworks for solar thermochemical applications, *Phys. Rev. Mater.* 2 (2018) 1–14, <https://doi.org/10.1103/PhysRevMaterials.2.095401>.
- [203] S.L. Dudarev, G.A. Botton, S.Y. Savrasov, C.J. Humphreys, A.P. Sutton, Electron-energy-loss spectra and the structural stability of nickel oxide: An LSDA+U study, *Phys. Rev. B* 57 (1998) 1505–1509, <https://doi.org/10.1103/PhysRevB.57.1505>.
- [204] V.I. Anisimov, J. Zaanen, O.K. Andersen, Band theory and Mott insulators: Hubbard U instead of Stoner I, *Phys. Rev. B* 44 (1991) 943–954, <https://doi.org/10.1103/PhysRevB.44.943>.
- [205] M. Cococcioni, S. de Gironcoli, A linear response approach to the calculation of the effective interaction parameters in the LDA+U method, *Phys. Rev. B* 71 (2005), <https://doi.org/10.1103/PhysRevB.71.035105>.
- [206] H. Tang, S. Neupane, Q. Yan, A. Ruzsinszky, Density functional theory study of controllable optical absorptions and magneto-optical properties of magnetic CrI₃ nanoribbons: implications for compact 2D magnetic devices, *ACS Appl. Nano Mater.* 5 (2022) 14388–14399, <https://doi.org/10.1021/acsnano.2c02722>.
- [207] W. Fu, J. Qiao, X. Zhao, Y. Chen, D. Fu, W. Yu, K. Leng, P. Song, Z. Chen, T. Yu, S.J. Pennycook, S.Y. Quek, K.P. Loh, Room temperature commensurate charge density wave on epitaxially grown bilayer 2H-tantalum sulfide on hexagonal boron nitride, *ACS Nano* 14 (2020) 3917–3926, <https://doi.org/10.1021/acsnano.0c00303>.
- [208] H. Peng, J.P. Perdew, Synergy of van der Waals and self-interaction corrections in transition metal monoxides, *Phys. Rev. B* 96 (2017), <https://doi.org/10.1103/PhysRevB.96.100101>.
- [209] D.O. Scanlon, B.J. Morgan, G.W. Watson, The origin of the enhanced oxygen storage capacity of Ce_{1-x}(Pd/Pt)_xO₂, *Phys. Chem. Chem. Phys.* 13 (2011) 4279, <https://doi.org/10.1039/c0cp01635g>.
- [210] H.V. Thang, E. Albanese, G. Pacchioni, Electronic structure of CuWO₄: dielectric-dependent, self-consistent hybrid functional study of a Mott-Hubbard type insulator, *J. Phys.: Condens. Matter* 31 (2019), <https://doi.org/10.1088/1361-648X/aaf3e>.
- [211] B. Hammer, J.K. Nørskov, *Advances in Catalysis*, 2000, pp. 71–129, [https://doi.org/10.1016/S0360-0564\(02\)45013-4](https://doi.org/10.1016/S0360-0564(02)45013-4).
- [212] M.R. Hestenes, E. Stiefel, Methods of conjugate gradients for solving linear systems, *J. Res. Natl. Bur. Stand.* 49 (1952) (1934) 409, <https://doi.org/10.6028/jres.049.044>.
- [213] D. Sheppard, R. Terrell, G. Henkelman, Optimization methods for finding minimum energy paths, *J. Chem. Phys.* 128 (13) (2008) 134106, <https://doi.org/10.1063/1.2841941>.

- [214] G.W. Watson, E.T. Kelsey, N.H. de Leeuw, D.J. Harris, S.C. Parker, Atomistic simulation of dislocations, surfaces and interfaces in MgO, *J. Chem. Soc., Faraday Trans.* 92 (1996) 433–438, <https://doi.org/10.1039/ft9969200433>.
- [215] K.M. Ho, C.L. Fu, B.N. Harmon, W. Weber, D.R. Hamann, Vibrational frequencies and structural properties of transition metals via total-energy calculations, *Phys. Rev. Lett.* 49 (1982) 673–676, <https://doi.org/10.1103/PhysRevLett.49.673>.
- [216] C.L. Fu, K.M. Ho, First-principles calculation of the equilibrium ground-state properties of transition metals: applications to Nb and Mo, *Phys. Rev. B* 28 (1983) 5480–5486, <https://doi.org/10.1103/PhysRevB.28.5480>.
- [217] A. De Vita, *The Energetics of Defects and Impurities in Metals and Ionic Materials from First Principles*, PhD Thesis, University of Keele, 1992, accessed August 23, 2022.
- [218] R.J. Needs, R.M. Martin, O.H. Nielsen, Total-energy calculations of the structural properties of the group-V element arsenic, *Phys. Rev. B* 33 (1986) 3778–3784, <https://doi.org/10.1103/PhysRevB.33.3778>.
- [219] H.J. Monkhorst, J.D. Pack, Special points for Brillouin-zone integrations, *Phys. Rev. B* 13 (1976) 5188–5192, <https://doi.org/10.1103/PhysRevB.13.5188>.
- [220] D. Santos-Carballal, A. Roldan, N.Y. Dzade, N.H. de Leeuw, Reactivity of CO₂ on the surfaces of magnetite (Fe₃O₄), greigite (Fe₃S₄) and mackinawite (FeS), *Philos. Trans. Roy. Soc. A: Math., Phys. Eng. Sci.* 376 (2018) 20170065, <https://doi.org/10.1098/rsta.2017.0065>.
- [221] J. Neugebauer, M. Scheffler, Adsorbate-substrate and adsorbate-adsorbate interactions of Na and K adlayers on Al(111), *Phys. Rev. B* 46 (1992) 16067–16080, <https://doi.org/10.1103/PhysRevB.46.16067>.
- [222] G. Makov, M.C. Payne, Periodic boundary conditions in ab initio calculations, *Phys. Rev. B* 51 (1995) 4014–4022, <https://doi.org/10.1103/PhysRevB.51.4014>.
- [223] M.A. Peck, D. Santos-Carballal, N.H. de Leeuw, M. Claeys, Density functional theory study of the adsorption of oxygen and hydrogen on 3d transition metal surfaces with varying magnetic ordering, *S. Afr. J. Chem.* 74 (2021) 69–72, <https://doi.org/10.17159/0379-4350/2021/v74a11>.
- [224] D. Santos-Carballal, A. Roldan, R. Grau-Crespo, N.H. de Leeuw, A DFT study of the structures, stabilities and redox behaviour of the major surfaces of magnetite Fe₃O₄, *Phys. Chem. Chem. Phys.* 16 (2014) 21082–21097, <https://doi.org/10.1039/c4cp00529e>.
- [225] A.E. Shields, D. Santos-Carballal, N.H. de Leeuw, A density functional theory study of uranium-doped thorium and uranium adatoms on the major surfaces of thorium dioxide, *J. Nucl. Mater.* 473 (2016) 99–111, <https://doi.org/10.1016/j.jnucmat.2016.02.009>.
- [226] O. Lupan, D. Santos-Carballal, N. Ababii, N. Magariu, S. Hansen, A. Vahl, L. Zimoch, M. Hoppe, T. Pauporté, V. Galstyan, V. Sontea, L. Chow, F. Faupel, R. Adelung, N.H. de Leeuw, E. Comini, TiO₂/Cu₂O/CuO multi-nanolayers as sensors for H₂ and volatile organic compounds: an experimental and theoretical investigation, *ACS Appl. Mater. Interface.* 13 (2021) 32363–32380, <https://doi.org/10.1021/acami.1c04379>.
- [227] M.J. Ungerer, D. Santos-Carballal, C.G.C.E. van Sittert, N.H. de Leeuw, Competitive adsorption of H₂O and SO₂ on catalytic platinum surfaces: a density functional theory study, *S. Afr. J. Chem.* 74 (2021) 57–68, <https://doi.org/10.17159/0379-4350/2021/v74a10>.
- [228] B. Ramogayana, D. Santos-Carballal, K.P. Maenetja, N.H. de Leeuw, P.E. Ngoepe, Density functional theory study of ethylene carbonate adsorption on the (0001) surface of aluminum oxide α -Al₂O₃, *ACS Omega* 6 (2021) 29577–29587, <https://doi.org/10.1021/acsomega.1c03771>.
- [229] O. Lupan, D. Santos-Carballal, N. Magariu, A.K. Mishra, N. Ababii, H. Krüger, N. Wolff, A. Vahl, M.T. Bodduluri, N. Kohlmann, L. Kienle, R. Adelung, N.H. de Leeuw, S. Hansen, Al₂O₃/ZnO heterostructure-based sensors for volatile organic compounds in safety applications, *ACS Appl. Mater. Interfaces* 14 (2022) 29331–29344, <https://doi.org/10.1021/acami.2c03704>.
- [230] M.J. Ungerer, D. Santos-Carballal, A. Cadi-Essadek, C.G.C.E. van Sittert, N.H. de Leeuw, Interaction of SO₂ with the Platinum (001), (011), and (111) surfaces: a DFT study, *Catalysts* 10 (2020) 558, <https://doi.org/10.3390/catal10050558>.
- [231] X. Wang, D. Santos-Carballal, N.H. de Leeuw, Oxygen diffusion in the orthorhombic FeNbO₄ material: a computational study, *Phys. Chem. Chem. Phys.* 25 (2023) 6797–6807, <https://doi.org/10.1039/D2CP04126j>.
- [232] B. Ramogayana, D. Santos-Carballal, K.P. Maenetja, K.T. Malatji, N.H. de Leeuw, P.E. Ngoepe, A DFT + U – D3 study of the adsorption of hydrogen fluoride and ethylene carbonate on the niobium-doped (001), (011), and (111) surfaces of lithium manganese oxide, *J. Electrochem. Soc.* 169 (9) (2022) 090507, <https://doi.org/10.1149/1945-7111/ac8e35>.
- [233] G. Henkelman, A. Arnaldsson, H. Jónsson, A fast and robust algorithm for Bader decomposition of charge density, *Comput. Mater. Sci.* 36 (2006) 354–360, <https://doi.org/10.1016/j.commatsci.2005.04.010>.
- [234] E. Sanville, S.D. Kenny, R. Smith, G. Henkelman, Improved grid-based algorithm for Bader charge allocation, *J. Comput. Chem.* 28 (2007) 899–908, <https://doi.org/10.1002/jcc.20575>.
- [235] W. Tang, E. Sanville, G. Henkelman, A grid-based Bader analysis algorithm without lattice bias, *J. Phys.: Condens. Matter* 21 (8) (2009), <https://doi.org/10.1088/0953-8984/21/8/084204>.
- [236] G. Henkelman, B.P. Uberuaga, H. Jónsson, A climbing image nudged elastic band method for finding saddle points and minimum energy paths, *J. Chem. Phys.* 113 (2000) 9901–9904, <https://doi.org/10.1063/1.1329672>.
- [237] G. Henkelman, H. Jónsson, Improved tangent estimate in the nudged elastic band method for finding minimum energy paths and saddle points, *J. Chem. Phys.* 113 (2000) 9978–9985, <https://doi.org/10.1063/1.1323224>.
- [238] J. Nocedal, Updating quasi-Newton matrices with limited storage, *Math. Comput.* 35 (1980) 773, <https://doi.org/10.2307/2006193>.
- [239] K. Momma, F. Izumi, VESTA 3 for three-dimensional visualization of crystal, volumetric and morphology data, *J. Appl. Crystallogr.* 44 (2011) 1272–1276, <https://doi.org/10.1107/S0021889811038970>.
- [240] V. Wang, N. Xu, J.-C. Liu, G. Tang, W.-T. Geng, VASPKIT: A user-friendly interface facilitating high-throughput computing and analysis using VASP code, *Comput. Phys. Commun.* 267 (2021), <https://doi.org/10.1016/j.cpc.2021.108033>.
- [241] OriginPro, 2019b, OriginLab Corporation, Northampton, MA, USA, n.d.
- [242] P.W. Tasker, The stability of ionic crystal surfaces, *J. Phys. C: Solid State Phys.* 12 (1979) 4977–4984, <https://doi.org/10.1088/0022-3719/12/22/036>.
- [243] A. Kiejna, T. Ossowski, T. Pabisiak, Surface properties of the clean and Au/Pd covered Fe₃O₄(111): DFT and DFT + U study, *Phys. Rev. B* 85 (2012), <https://doi.org/10.1103/PhysRevB.85.125414>.
- [244] Y.-X. Huang, S.-W. Xu, X.-H. Yang, Weak electrostatic field orientation of cold KRb molecules enhanced by a shaped laser pulse, *Chin. Phys. Lett.* 30 (8) (2013), <https://doi.org/10.1088/0256-307X/30/8/083701>.
- [245] B. Friedrich, D.R. Herschbach, On the possibility of orienting rotationally cooled polar molecules in an electric field, *Z. Phys. D Atoms, Mol. Clusters* 18 (1991) 153–161, <https://doi.org/10.1007/BF01437441>.
- [246] H.J. Loesch, A. Remscheid, Brute force in molecular reaction dynamics: a novel technique for measuring steric effects, *J. Chem. Phys.* 93 (1990) 4779–4790, <https://doi.org/10.1063/1.458668>.
- [247] F. Che, J.T. Gray, S. Ha, J.-S. McEwen, Improving Ni catalysts using electric fields: a DFT and experimental study of the methane steam reforming reaction, *ACS Catal.* 7 (2017) 551–562, <https://doi.org/10.1021/acscatal.6b02318>.
- [248] N. Kruse, G. Abend, J.H. Block, The kinetics of adsorption and thermal desorption of NO on stepped Pt single crystal surfaces, *J. Chem. Phys.* 88 (1988) 1307–1312, <https://doi.org/10.1063/1.454201>.
- [249] P. Deshlahra, E.E. Wolf, W.F. Schneider, A periodic density functional theory analysis of CO chemisorption on Pt(111) in the presence of uniform electric fields †, *J. Phys. Chem. A* 113 (2009) 4125–4133, <https://doi.org/10.1021/jp810518x>.
- [250] N.W. Ashcroft, N.D. Mermin, *Solid State Physics*, Holt, Rinehart and Winston, New York; London, 1976.
- [251] J. Liang, Q. Yu, X. Yang, T. Zhang, J. Li, A systematic theoretical study on FeO_x-supported single-atom catalysts: M₁/FeO_x for CO oxidation, *Nano Res.* 11 (2018) 1599–1611, <https://doi.org/10.1007/s12274-017-1775-0>.
- [252] D.H. Gibson, Carbon dioxide coordination chemistry: metal complexes and surface-bound species. What relationships?, *Coord. Chem. Rev.* 185–186 (1999) 335–355, [https://doi.org/10.1016/S0010-8545\(99\)00021-1](https://doi.org/10.1016/S0010-8545(99)00021-1).
- [253] D.H. Gibson, The organometallic chemistry of carbon dioxide, *Chem. Rev.* 96 (1996) 2063–2096, <https://doi.org/10.1021/cr940212c>.
- [254] M. Aresta, A. Dibenedetto, E. Quaranta, CO₂ Coordination to Metal Centres: Modes of Bonding and Reactivity, in: M. Aresta, A. Dibenedetto, E. Quaranta (Eds.), *Reaction Mechanisms in Carbon Dioxide Conversion*, Springer Berlin Heidelberg, Berlin, Heidelberg, 2016, pp. 35–69, https://doi.org/10.1007/978-3-662-46831-9_2.
- [255] A. Roldan, N.H. de Leeuw, Methanol formation from CO₂ catalyzed by Fe₃S₄(111): formate versus hydrocarboxyl pathways, *Faraday Discuss.* 188 (2016) 161–180, <https://doi.org/10.1039/C5FD00186B>.